# CJRB-101, a live biotherapeutic product, stimulates macrophage-T cell crosstalk and improves anti-tumor activity in advanced non-small cell lung cancer

Jii Bum Lee

**The Graduate School**
**Yonsei University**
**Department of Medicine**

# CJRB-101, a live biotherapeutic product, stimulates macrophage-T cell crosstalk and improves anti-tumor activity in advanced non-small cell lung cancer

**A Dissertation Submitted**
**to the Department of Medicine**
**and the Graduate School of Yonsei University**
**in partial fulfillment of the**
**requirements for the degree of**
**Doctor of Philosophy in Medical Science**

**Jii Bum Lee**

**June 2024**

**This certifies that the Dissertation of Jii Bum Lee is approved.**

Byoung Chul Cho

Thesis Supervisor

Hyo Sup Shim

Thesis Committee Member

Sun Min Lim

Thesis Committee Member

Kyoung-Ho Pyo

Thesis Committee Member

Kwang Ho Lee

Thesis Committee Member

**The Graduate School**
**Yonsei University**
**June 2024**

# ACKNOWLEDGEMENTS

I am very much delighted to graduate and reflect on the people who have encouraged me throughout my endeavors. This doctoral dissertation is a statement to the wonderful scientists and collaborators who are relentlessly researching to end cancer.

First of all, I thank Professor Byoung Chul Cho who is the source of inspiration to many of the work that I do. Without you, I would never have dreamed of becoming a thoracic oncologist, to have passion for translational research, and to be the person I am today. Thank you for your inspiration, encouragement, and unwavering support.

I am also grateful to Professor Hyo Sup Shim who was my thesis supervisor. As a renowned pathologist, he has been helpful to me many times, and I can count on him for the right diagnosis.

To Professor Lim: I am always astounded by your energy and ease which you have as a doctor and researcher. You are the guiding light to who I should become. Thank you for your inspiration every day.

To Dr. Kyoung-Ho Pyo: This dissertation would never have come to light if it wasn't for your leadership and scrutiny into details. Thank you for guiding me. I am forever grateful to you.

To Dr. Lee Kwang Ho for the thorough comments and passion for research. Thank you for making this possible.

There are many people that I am thankful in DAAN Lab, including Professor Min Hee Hong, Dr. Mi Ran Yun, Dr. Mira Yu, Dr. Jae Hwan Kim and

Dr. Sewon Park.

I want to send my greatest thanks to all the researchers who have spent their time and energy for this project. I am truly grateful for Dr. Seong-San Kim, Sujeong Baek, Arim Min, Bo-eun Kown, and Junwon Yang for their passion, knowledge and commitment to this project. Also, a special thanks to Sujin Choi for her encouragement and support throughout the years.

Finally, I want to share the joy of my graduation with my family members, including dad, mom, Joseph, John, and Jonah. I thank God for giving me the best gift that I could possibly ever have. Thank you for your prayers. This doctoral dissertation is dedicated to my dad, who taught me to be the person I am today.

2024.06

# TABLE OF CONTENTS

# LIST OF FIGURES

# LIST OF SUPPLEMENTARY FIGURES

# LIST OF SUPPLEMENTARY TABLES

## ABSTRACT

# CJRB-101, a live biotherapeutic product, stimulates macrophage-T cell crosstalk and improves anti-tumor activity in advanced non-small cell lung cancer

**Background:** The microbiota influences the response to immune checkpoint inhibitors (ICIs); however, little is known about the efficacy of live biotherapeutic products (LBPs) in combination with pembrolizumab in advanced non-small cell lung cancer (NSCLC). Here, we reveal that a high-diversity enterotype is associated with the clinical response to pembrolizumab in treatment-naïve, metastatic NSCLC.

**Methods:** To modulate the immune environment in the gut microbiota, CJRB-101, a live biotherapeutic product containing a strain belonging to *Leuconostoc mesenteroides* was selected from among 355 strains.

**Results:** CJRB-101 effectively reduced tumor growth in humanized NSCLC patient-derived xenograft models by repolarizing M2 to M1 macrophages, thereby enhancing active $CD8^+$ $T_c$ cells in the tumor microenvironment (TME) and triggering the adaptive immune system via the gut-TME axis.

**Conclusions:** Taken together, CJRB-101 in combination with pembrolizumab is a potential therapeutic strategy.

**Clinical Relevance:** CJRB-101 improves anti-tumor effects in NSCLC by LBP-driven immunomodulation of macrophages and enhances tumor killing capacity of immune cell through the gut-TME axis.

---

Key words : CJRB-101, live biotherapeutic product, non-small cell lung cancer, immunotherapy

# 1. Introduction

Non-small cell lung cancer (NSCLC) has the highest cancer-related mortality rate worldwide [1-3]. Pembrolizumab, an anti-programmed cell death protein 1 (anti-PD-1) agent, with or without chemotherapy, is the standard treatment of choice for metastatic squamous and non-squamous NSCLC without driver alterations [4]. Depending on programmed death ligand-1 PD-L1 expression, defined as the tumor proportion score (TPS), patients are either treated as monotherapy (TPS≥50%) or in combination with chemotherapy (TPS 50% or less). Despite the proven durable response to pembrolizumab, with improved progression-free survival (PFS) and overall survival (OS), the 5-year survival rate is approximately 20% [5,6]. Thus, identifying mechanisms to overcome resistance to ICIs, including anti-PD-1 agents, is of paramount importance.

Recent studies have shown that crosstalk between the gut microbiota and host immune cells plays an important role in the modulation of the immune system in patients with cancer, both locally and systemically within the host [7]. Changes in the composition of the microbial communities in the gut are associated with the efficacy of ICIs and may be responsible for the variability in the PD-1/PD-L1 immunotherapy response in human cohorts and preclinical models [8-11]. Routy et al. [12] and Gopalakrishnan et al. [11] reported that specific bacterial species were present in relatively higher abundance within the gut microbiome of responders receiving anti-PD-1 treatment, and that replenishing these species contributed to restoring the efficacy of PD-1 inhibition in preclinical mouse models.

CJRB-101 is a live biotherapeutic product containing a strain of *Leuconostoc mesenteroides. Leuconostoc* belongs to the family of gram-positive bacteria *Lactobacillaceae*, a diverse group of strains, including lactic acid bacteria (LAB), commonly found in fermentative foods.

In this study, we provide a comprehensive analysis of the microbiome landscape and immune biomarkers in patients with advanced NSCLC treated with pembrolizumab, with or without chemotherapy. We also investigated key immunomodulatory changes and biomarkers of immune cells that distinguish the anti-tumor efficacy of the combination therapy of CJRB-101 plus pembrolizumab from that of pembrolizumab monotherapy.

# 2. MATERIALS AND METHODS

## 2.1. Patients

Patients were recruited for the CJ microbiome cohort (pembrolizumab with or without chemotherapy) and a phase 1/2 trial assessing the safety, efficacy, and preliminary efficacy of CJRB-101 (low dose) in combination with pembrolizumab (NCT05877430). In both studies, patients aged 20 years or older and histologically confirmed, treatment-naïve, stage IV NSCLC without sensitizing EGFR or ALK mutations, Eastern Cooperative Oncology Group performance status of 0 or 1, adequate organ function, and at least one measurable lesion according to the Response Evaluation Criteria in Solid Tumor version 1.1 (RECIST v 1.1) were enrolled. Patients were excluded if they had prior exposure to PD-1 or PD-L1 inhibitors, previous allogenic organ transplant, or history of major surgery within 28 days prior to treatment.

## 2.2 Trial design and treatment

In the CJ microbiome cohort, patients with PD-L1 expression >50% received pembrolizumab at a fixed dose of 200 mg every 3 weeks for up to 35 cycles, irrespective of histology (non-squamous or squamous). In addition to pembrolizumab, patients with squamous histology and PD-L1 <50% received four cycles of carboplatin (area under the concentration-time curve (AUC), 5 mg/m$^2$) and pemetrexed (500 mg per square meter) every 3 weeks. Patients with non-squamous histology and PD-L1 <50% received four cycles of carboplatin (AUC 5 mg/m$^2$) and paclitaxel (200 mg/m$^2$). All treatments were administered intravenously for 3-week cycles. In a phase 1/2 trial of the treatment-naive NSCLC cohort, the patient was treated with CJRB-101 administered at 1 capsule daily (low dose) in combination with pembrolizumab.

Patients were also given premedication, including folic acid, vitamin $B_{12}$, and glucocorticoids for pemetrexed-treated patients and glucocorticoids and antihistamines for paclitaxel-treated patients. Dose reduction was not permitted for pembrolizumab, but treatment could be interrupted, delayed, or discontinued based on tolerability. Dose reduction for pemetrexed, paclitaxel, and carboplatin was permitted at two levels of dosage, and dose interruption and discontinuation were followed as per the protocol. Patients were treated until disease progression, unacceptable adverse events, investigator decision, or patient decision to discontinue the treatment.

## 2.3 Assessment

PD-L1 expression was analyzed using the PD-L1 IHC 22C3 pharmDx antibody (clone 22C3, Dako North America, Inc., Carpinteria, CA, USA) in FFPE tumor samples obtained by biopsy or resected at the time of initial diagnosis. PD-L1 expression was categorized by the percentage of TPS, which was defined as the percentage of PD-L1 staining in tumor cells. Archival tissue was collected during screening for whole exome sequencing (WES) and bulk-RNA sequencing. Stool collection for microbiome analysis was performed at screening, after cycle 2, day 1 (C2D1), and during progression. Treatment response was evaluated using chest and abdominal computed tomography (CT) scanning, which was performed for weeks 6 and 12, and then every 9 weeks thereafter. Tumor response was assessed using Response Evaluation Criteria in Solid Tumor version 1.1 (RECIST v 1.1). Patients were followed-up every 12 weeks to assess their survival. Treatment-related adverse events were reported according to the Common Terminology Criteria for Adverse Events v5.0.

## 2.4 Assessment of the clinical efficacy of pembrolizumab with or without chemotherapy

Patients were enrolled between November 2022 and November 2023. The primary outcome was objective response (responder), defined by radiographic evidence of complete response, partial response, and stable disease for at least 6 months. A lack of clinical response (non-responder) was defined as progressive disease (PD) and stable disease for less than 6 months. Progression-free survival (PFS) was defined as the time from the start of treatment to PD or death. Overall survival (OS) was defined as the time from the start of treatment to death from any cause. The data cutoff was November 2023, and patients without a known date of death were censored at the time of the last follow-up. This study was conducted in accordance with the International Conference on Harmonization Guidelines on Good Clinical Practice and the Declaration of Helsinki. All participants provided written informed consent, and the protocol was approved by the Institutional Review Board of Yonsei Cancer Center (IRB 4-2022-0355 for the CJ microbiome cohort; IRB 4-2023-0715 for the phase 1/2 study).

## 2.5 Luminex assay for measurement of cytokine

The concentration of cytokines was measured in the patients' plasma using the NHP XL Cytokine Luminex® Performance Premixed Kit (FCSTM18B-29, R&D Systems) following the manufacturer's instructions. Briefly, the microparticle cocktail, plasma, and biomarker standards were added to a 96-well plate and incubated for 2 h. The plates were washed and a biotin antibody cocktail was added. Following a 1 hour incubation, the plates were washed and streptavidin-phycoerythrin (PE) was added for 30 min, followed by a final wash and resuspension in wash buffer. All incubations were performed at room temperature on a microplate shaker at 800 RPM.

## 2.6 Single-cell RNA sequencing

The tumor samples were dissociated and prepared using single-cell library kits (10X Genomics, 5' end chromium) for single-cell RNA sequencing (Macrogen, Korea). After quality check of the cDNA, the depth of sequencing read was defined depending on the quality and cell count of the cells. Additional sequencing to increase depth was requested after initial inspection of the UMI and read counts. Sequencing data was then processed using the 10x Genomics Cell Ranger 7.0.1 multi pipeline(17). Pre-built GRCh38 and mm10 reference transcriptomes were used. Single-cell RNA sequencing data were analyzed using 'Seurat' in R and 'Scanpy' in Python. Cells with more than 90% human gene abundance, less than 20% mitochondrial gene abundance, and a minimum of 100 genes were retained, and genes with a minimum of three cells were retained. Cell doublets were identified by 'Scrublet' and removed. Cell types were identified by initially mapping single cell profiles to the Azimuth human lung reference version 1, followed by manual re-annotation. For downstream analysis, we used 'presto,' 'dittoSeq' and 'EnhancedVolcano' packages in R and Monocle 3. To conduct gene enrichment analysis, we utilized the ClueGO (version 2.5.8) module in Cytoscape (version 3.9.0). The reference database was derived from the Gene Ontology (GO) immune system process, excluding annotations inferred from electronic sources. The parameters were set as follows: the threshold for the minimum number of genes in each term was set at 3, and the GO tree interval was defined within a range of 3 to 8. Statistical options included enrichment/depletion using a two-sided hypergeometric test, and the Benjamini-Hochberg correction was applied for multiple comparisons.

## 2.7 Gut microbiome analysis

Total DNA was extracted from the fecal samples using the FastDNA Spin kit (MP Biomedicals) or Maxwell RSC PureFood GMO and Authentication Kit (Promega), according to the manufacturer's instructions. For amplicon sequencing data, polymerase chain reaction (PCR) amplification of the V3 to V4 regions of the 16S rRNA gene was performed using primers 341F (CCTACGGGNGGCWGCAG) and 805R (GACTACHVGGGTATCTAATCC). Amplifications were carried out under the following conditions: initial denaturation at 95°C for 3 min, followed by 25 cycles of denaturation at 95°C for 30 s, primer annealing at 55°C for 30 s, and extension at 72°C for 30 s, with a final elongation at 72°C for 5 min. The PCR product was confirmed using 1% agarose gel electrophoresis and visualized using a Gel Doc system (Bio-Rad). The amplified products were purified by CleanPCR (CleanNA). Equal concentrations of purified products were pooled, and short fragments (non-target products) were removed using CleanPCR (CleanNA). Quality and product size were assessed on a Bioanalyzer 2100 (Agilent) using a DNA 7500 chip. Mixed amplicons were pooled and sequencing was carried out at CJ Bioscience, Inc. with the Illumina MiSeq Sequencing system according to the manufacturer's instructions.

Taxonomic profiling of amplicon sequencing data was performed using QIIME2 (Version 2022.11)(18). Primer sequences were removed using the trim-paired method from the Cutadapt plugin in QIIME2, and untrimmed reads were discarded. Paired-end reads were truncated and merged, and chimeric sequences were removed from the dada2 plugin in QIIME2 using the denoise-paired method (19). The classify-consensus-search method from the feature-classifier plugin in QIIME2 was used to assign taxonomy to the resulting amplicon sequence variants (ASVs) against the EzBioCloud database(20-22). Each sequence was assigned to the top hit based on a 97% identity threshold and minimum coverage of 80%. In cases where there were multiple equally scored top hits in the taxonomic assignment result, the sequence was assigned to the last common ancestor of all hits, with the suffix '_uc, indicating' unclassified.'

For the downstream analysis, we used the 'microbiome, ' 'phyloseq,' 'presto' and 'vegan' packages in R(23). Taxonomic profiles from amplicon sequencing data were used to create phyloseq objects. We used LEfSe to identify differentially abundant taxa between the responders and non-responders. For enterotyping, we employed Dirichlet multinomial mixture (DMM) community typing to cluster microbial community profiling data at the genus level. The plots were drawn using

the ‘ggplot2,’ ‘ggpubr’ and ‘RColorBrewer’ packages in R. Heatmaps were generated using Morpheus (https://software.broadinstitute.org/morpheus).

## 2.8 Bacterial genome analysis

Average nucleotide identity (ANI) was calculated using nucleotide sequences from the type strains of *Leuconostoc mesenteroides* subspecies *Leuconostoc citreum*, *Lactobacillus delbrueckii*, CJRB-101, CJRS-10672, CJRS-17429, and CJRS-17430 with MMSeqs2(24). The number of genes in each genome was determined using Prodigal software (25).

## 2.9 Bacteria preparation for selection of a LBP candidate strain, CJRB-101

Stored stocks of 355 bacterial strains were thawed 2 d before the experiment. An aliquot of 100 μL of each suspension was inoculated into 10 mL of culture medium suitable for each strain: MRS (288130, BD), TSB (MB-T1053, MBcell), and BL (MB-B1062, MBcell) for 19-20 hours at 37ºC. Cultured broth (100 μL) was inoculated into 10 mL of culture medium and incubated for 19-20 hours at 37ºC. The cells were then centrifuged at 4000 RPM for 20 min at room temperature. The supernatant was discarded and the cell pellets were washed twice with phosphate buffer saline (PBS) (10010-023, Gibco). Cell numbers were calculated using Novocyte (Agilent, Santa Clara, CA, USA). A portion of the cell suspension was heat-killed at 95 °C for 20 min, and the remaining portion was used as the live bacteria. Live and heat-killed bacterial cells were suspended in immune cell culture medium and the cell number was prepared according to the ratio of immune cells to bacterial cells (1:10) for the co-culture experiment.

## 2.10 Cell lines

### 2.10.1 Raw264.7

Raw264.7, a mouse monocyte/macrophage cell line, was cultured in DMEM (11995-065, Gibco) supplemented with 10% FBS (16000-044, Gibco) and 1% anti-anti (15240-062,Gibco). Raw264.7 cells ($6 \times 10^4$ cells/well) were seeded 24 h before the experiment in a 96-well plate and incubated at 37 °C in a 5% $CO_2$ incubator. After incubation for 24 h, the medium was removed and the cells were washed with PBS. An aliquot of 200 μL of bacteria ($6 \times 10^5$/well) suspended in DMEM supplemented with 10% FBS was then added. After incubation for 24 h, the supernatant was

transferred to a 96-well round-bottom plate and centrifuged at 1500 RPM for 3 min at room temperature. The harvested supernatant was used to measure the concentrations of cytokines (IL-6 and IL-1β).

### 2.10.2 THP-1

THP-1, a human monocytic leukemia cell line, was cultured in RPMI supplemented with 10% FBS, 1% anti-anti, and 0.05 mM 2-mercaptoethanol (M6250-500ML, Sigma). THP-1 cells (8 × $10^4$ cells/well) were seeded with 25 ng/mL PMA (P8139, Sigma) 48 h before the experiment in a 96-well plate and were incubated at 37 °C in a 5% $CO_2$ incubator. After incubation for 48 h, the medium was removed, and the cells were washed with PBS. Bacteria (200 μL, 8 x $10^5$/well) were suspended in RPMI medium supplemented with 10% FBS. After incubation for 24 h, the supernatant was transferred to a 96-well round-bottom plate and centrifuged at 1500 RPM for 3 min at room temperature. The harvested supernatant was used to measure the levels of cytokines (IL-6 and IL-1β).

## 2.11 Mouse splenocytes

Mouse splenocytes were obtained from C57BL/6 mice. The spleen was flushed using a 25G needle in HBSS (14175-095, Gibco) with collagenase IV (17104-019, Gibco) and incubated for 25 min at 37 °C in a 5% $CO_2$ incubator. 1 mM EDTA (AM9260G, Invitrogen) was added and the mixture was incubated for 5 min at 37 °C in a 5% $CO_2$ incubator. The cells were then centrifuged at 1500 RPM for 3 min at room temperature. Red blood cells were lysed with 1x RBC lysis buffer (00-4333-57, Invitrogen) for 2 min at room temperature and RPMI (22400-089, Gibco) supplemented with 10% FBS was added. The cells were then centrifuged at 1500 RPM for 3 min at room temperature. The cell pellet was resuspended in RPMI medium supplemented with 10% FBS and filtered using a cell strainer. Splenocytes (5 × $10^5$ cells/well) were seeded, and 100 μL of bacteria (5 × $10^6$/well) suspended in RPMI supplemented with 10% FBS was added. After incubation for 24 h, the supernatant was transferred to a 96-well round-bottom plate and centrifuged at 1500 RPM for 3 min at room temperature. The harvested supernatant was used to measure cytokine (IFNγ).

To detect T cell markers, splenocytes were seeded at a density of 5 × $10^5$ cells/well in 96-well plates pre-coated with 0.1 μg/ml anti-CD3 (553057, BD Biosciences) and supplemented with 1 μg/mL soluble anti-CD28 (553294, BD Biosciences). An aliquot of 100 μL of bacteria (5x$10^6$/well)

suspended in RPMI medium supplemented with 10% FBS was added. After 48 h of incubation, intracellular cytokine staining was performed. GolgiSTOP (51–2092 KZ, BD Biosciences) and GolgiPLUG (51–2301 KZ, BD Biosciences) were added and incubated for 3 h at 37 °C in a 5% $CO_2$ incubator. The cell pellet was resuspended, transferred to a 96-well round bottom plate, and then centrifuged at 1500 RPM for 3 min at room temperature. The cell pellet was washed with PBS and centrifuged at 1500 RPM for 3 min at room temperature. The cell surface was stained with anti-CD3 (560592; BD Biosciences), anti-CD4 (560181; BD Biosciences), and anti-CD8 (551182; BD Biosciences) for 20 min at 4 °C. The cells were fixed and permeabilized using a BD Cytofix/Cytoperm kit (554714, BD Biosciences) and stained with anti-IFNγ (564336, BD Biosciences) for 20 min at 4 °C. Cells were resuspended in PBS with 2% FBS and analyzed using a FACSLyric instrument (BD Biosciences, Franklin Lakes, NJ, USA).

## 2.12 Cytokine (CBA)

Measurement of IL-6, IL-1 β and IFNγ levels was performed with the samples obtained as described above using a Cytometric Bead Array (CBA) Kit (BD Biosciences, San Jose, CA) according to the manufacturer's instructions: Mouse IL-6 CBA Flex Set (558301, BD), Mouse IL-1β CBA Flex Set (560232, BD), Mouse IFNγ CBA Flex Set (558296, BD), Human IL-6 Flex Set (558276, BD), and Human IL-1β (558279, BD). The CBA data were acquired using a FACSLyric instrument (BD Biosciences, Franklin Lakes, NJ, USA). The FCS file was analyzed using the FCAP Array (version 3.0.1 for Windows). *Bifidobacterium bifidum* (*B. bifidum*) was used as the positive control(26). The concentration of cytokines was converted into a $\log_2$ fold change and compared to the amount of heat-killed *B. bifidum*.

## 2.13 Human peripheral blood mononuclear cells

Human peripheral blood mononuclear cells PBMCs (700252, STEMCELL Technologies) were purchased from STEMCELL Technologies. PBMCs were seeded at a density of $2 \times 10^5$ cells/well in 96-well plates pre-coated with 0.1 μg/ml anti-CD3 and supplemented with 1 μg/mL soluble anti-CD28. One hundred microliters of bacteria ($2 \times 10^6$/well) suspended in RPMI supplemented with 10% FBS were added. After incubation for 24 hours, intracellular cytokine staining was performed. GolgiSTOP and GolgiPLUG were added and the cells were incubated for 3 h at 37 °C in a 5% $CO_2$ incubator. The cell pellet was resuspended, transferred to a 96-well round

bottom plate, and then centrifuged at 1500 RPM for 3 min at room temperature. The cell pellet was washed with PBS and centrifuged at 1500 RPM for 3 min at room temperature. The cell surface was stained with anti-CD3 (563800; BD Biosciences) and anti-CD8 (566855; BD Biosciences) for 20 min at 4 °C. The cells were fixed and permeabilized using a BD Cytofix/Cytoperm kit (554714, BD Biosciences) and stained with anti-IFNγ (566394, BD Biosciences) for 20 min at 4 ℃. Cells were resuspended in FACS buffer (PBS with 2% FBS) and analyzed using a FACSLyric instrument (BD Biosciences, Franklin Lakes, NJ).

## 2.14 In vivo assays

### 2.14.1 Syngeneic mouse model

A syngeneic mouse model of Lewis lung carcinoma (LLC1) was used to evaluate the anti-tumor effect of bacteria (CJRS-17429, CJRS-17430, CJRB-101, and CJRS-10672) and anti-PD-1. LLC1 cells ($4 \times 10^5$) were implanted subcutaneously in C57BL/6 female mice (7-weeks age). Treatment with bacteria and anti-PD-1 was initiated when the tumor size reached almost 30-50 $mm^3$. Bacteria (CJRS-17429, CJRS-17430, CJRB-101, and CJRS-10672) were administered daily (QD) at 1 x $10^6$/mouse via oral gavage. And anti-PD-1 (BP0146, BioXCell) was administered thrice a week at a dose of 10 mg/kg via intraperitoneal injection. Tumor size was measured using Vernier calipers three times per week until the end of the experiment. The equation for tumor volume was 'length×width$^2$×0.532'. The mice were sacrificed one day after the last treatment.

C3PQ (lung squamous cell carcinoma) was used to evaluate the combination of CJRB-101 and anti-PD-1. BALB/C female mice (7-weeks of age) were implanted subcutaneously on the right flank with $1 \times 10^6$ syngeneic C3PQ cells. The tumor size was measured daily using Vernier calipers. Body weights were measured 2 times per week.

### 2.14.2 Preparation of humanized PDX models

YHIM-2003, YHIM-2004, YHIM-2009, and YHIM-2014 are PDX models originating from NSCLC patients who have undergone surgery at Yonsei Cancer Center. This patient had a history of smoking and high PD-L1 expression in the primary tumor. The macrophage infiltration rate was high, but the $CD8^+$ $T_c$ cell infiltration rate was moderate. The genomic profiles of each PDX model were analyzed using whole-exome sequencing. The somatic

mutation is referred to as normal-matched blood DNA. The mutation calling algorithm was GATK4, and the criterion for mutation was VAF >5%. Frameshift, indel, missense, gene amplification, and nonsense deletion mutations were analyzed.

### 2.14.3 Drug treatment

CJRB-101, a microbiome agent provided by CJ Bioscience, was diluted with PBS to prepare $1x10^9$ CFU per 100 μL and administered within 24 h. The animals were orally administered twice a day (BID). The cell membrane (CM, provided by CJ Bioscience) was administered once every two days at 50 mg/kg via intraperitoneal injection (*i.p.*, Q2D). Pembrolizumab (Keytruda, MSD) was administered once every five days at 10 mg/kg (*i.p.*, Q5D). Mouse anti-PD-1 (BP0146, BioXcell) was administered twice per week at 10 mg/kg (*i.p.*, BIW). The TLR4 inhibitor, Resatorvid (TAK-242, S7455, Selleckchem), was administered once a day at a dose of 2 mg/kg (*i.p.*, QD).

## 2.15 Immune cell depletion assay

Cellular subsets were depleted by administering 400 μg/head of antibodies as follows: anti-CD8-α (clone 2.43, Leinco Technologies, Missouri), anti-Ly-6G/Ly-6C (clone RB6-8C5, Leinco Technologies) twice a week. Macrophages were depleted every other day using 300 μg anti-CD115 (clone ASF98, Leinco Technologies) every other day.

## 2.16 Immune profiling using flow cytometry analysis

Tumor cells were collected from in vivo models and enzymatically dissociated into single cells using a mechanical enzymatic dissociation system (gentleMACS, Miltenyi Biotec, Bergisch Gladbach, Germany). Tumors were cut into small fragments 2–4 mm in length and placed in gentle MACS tubes containing the enzyme mixture. Tumor fragments and the enzyme mix were dissociated using a gentleMACS dissociator and incubated for 30 min at 37°C under continuous rotation. This step was repeated three times using different GentleMACS dissociator programs. Then, it was filtered through a 70-μm cell strainer. Tumors were harvested from BALB/C and C57BL/6 syngeneic mice, enzymatically dissociated into single cells with collagenase type I (Worthington Biochemical, Lakewood, NJ) for 1 h at 37°C in a shaking incubator (DAIHAN Scientific, Wonju, Korea), and filtered through a 70-μm cell strainer. Mouse intestines were dissociated using the Lamina propria dissociation kit (130-097-410, Miltenyi Biotec) and a gentleMACS dissociator. Cells were washed with FACS buffer (PBS containing 3% BSA, 0.01% sodium azide, and 1 mM

EDTA) and blocked with FcR Blocking Reagent (101320, BioLegend, San Diego, CA) at 4°C for 20 min. After fixation, the cells were stained with True-Nuclear transcription factor buffer (424401, BioLegend) at room temperature for 30 min. For tumor cells and splenocytes of humanized mice, the T cell population was stained with anti-CD45 (304032; BioLegend), anti-CD45RA (304142; BioLegend), anti-CD28 (302948; BioLegend), anti-IFNγ (502542; BioLegend), anti-Ki-67 (151212; BioLegend), anti-CD56 (12-0567-42; BioLegend), anti-FoxP3 (320126; BioLegend), anti-CD4 (300528; BioLegend), anti-CD3e (300420; BioLegend), anti-CCR7 (353214; BioLegend), anti-CD8a (301028; BioLegend), anti-CD25 (356122; BioLegend) antibodies. The myeloid cell populations were identified using anti-CD45 (304032; BioLegend), anti-CD206 (740180; BioLegend), anti-CD80 (305225; BioLegend), anti-CD86 (305428; BioLegend), anti-HLA-DR (307644; BioLegend), anti-CD11c (301644; BioLegend), anti-Ki-67 (151212; BioLegend), anti-CD68 (333808; BioLegend), anti-CD14 (367110; BioLegend), anti-CD19 (302216; BioLegend) for B cells, anti-CD11b (302216; BioLegend), and anti-CD15 (301920; BioLegend) antibodies. For tumor cells and splenocytes from syngeneic mice, the T cell and myeloid cell populations were stained with anti-CD11c (117330; BioLegend), anti-CD14 (123323; BioLegend), anti-Ly-6G (127641; BioLegend), anti-CD8a (100750; BioLegend), anti-CD49b (108906; BioLegend), anti-EMR1 (157304; BioLegend), anti-CD45 (103132; BioLegend), anti-CD3e (100320; BioLegend), anti-CD19 (115512; BioLegend), and anti-CD4 (100526; BioLegend) antibodies. T cell and myeloid cell in intestine was stained with Live/Dead staining (Zombie Aqua 423102, BioLegend), anti-CD11c (117330; BioLegend), anti-TCR-$\gamma/\delta$ (118129; BioLegend), anti-Ly-6G (127641; BioLegend), anti-CD4 (100550; BioLegend), anti-CD45 (103149; BioLegend), anti-CD49b (108906; BioLegend), anti-EMR1 (157304; BioLegend), anti-TCR-β (109240; BioLegend), anti-CD11b (101228; BioLegend), anti-CD19 (115512; BioLegend) antibodies. Multicolor flow cytometry analysis was performed using a BD LSR-fortessa™ X-20 instrument (BD Biosciences, Franklin Lakes, NJ). FlowJo software v10 (Tree Star, Ashland, Orlando) was used for data acquisition and analysis.

## 2.17 Tumor microenvironment analysis

### 2.17.1 Multiplexed Immunohistochemistry (mIHC)

For multiplexed immunohistochemical staining of the sections, BOND RX Fully Automated Research Stainer (21.2821; Leica Biosystems, Nubloch, Germany) and an Opal Polaris

7 Color IHC Detection Kit (P-000003, Akoya Biosciences, Massachusetts) were used. All procedures were performed according to the manufacturer's instructions. In summary, deparaffinized sections were incubated with citrate- or Tris-based antigen-unmasking solutions (for heat-induced epitope retrieval) at 98 °C for 20 min. They were then treated with hydrogen peroxide and a protein-blocking reagent to prevent nonspecific binding of the antibodies to the sections. Sections were sequentially treated with primary antibodies, horseradish peroxidase (HRP)-conjugated antibodies, and specific fluorophores to detect the proteins of interest. Multiple staining rounds were performed using the following anti-human antibodies: anti-CD68 (76437, Cell Signaling Technology, Massachusetts, USA), anti-PD-L1 (ACI 3171A, Cell Signaling Technology), anti-granzyme B (Cell Signaling Technology), anti-CD16 (24326, Cell Signaling Technology), anti-CD11c (45581, Cell Signaling Technology), anti-CD4 (ab181724, Abcam, Cambridge, United Kingdom), anti-CD8 (CD8-4B11-L-CE, Leica Biosystems), anti-PD-1 (ab137132, Abcam), anti-FoxP3 (98377; Cell Signaling Technology), and anti-PanCK (AE1/AE3-601-L-CE; Leica Massachusetts, US Biosystems). Tissue sections were counterstained with Spectral DAPI (4′,6-diamidino-2-phenylindole; FP1490; Akoya Biosciences).

### 2.17.2 Imaging analysis

Images of whole tissue contents were generated using whole-slide scanning with a Vectra Polaris Automated Quantitative Pathology Imaging System (CLS143455, Akoya Biosciences). Multispectral images for analysis were defined and selected within the whole tissue using the Phenochart whole-slide contextual viewer software (version 1.12, Akoya Biosciences). InForm software (version 2.6, Akoya Biosciences), equipped with an integrated algorithm for tissue analysis, was employed to transform the multispectral image data into numerical data. These data encompassed both numerical and spatial information regarding the tumor nest and stromal region, defining the cell components (nuclear, cytosolic, and membrane margins), classifying the cell populations, and the intensities of each marker. Cell populations were discerned based on distinctive patterns of CD marker expression, each exhibiting unique cellular properties, such as nuclear, cytosolic, and membrane sizes and shapes (CD4 and CD8 for T cells, CD68 for macrophages, Pan-CK for epithelial cells or cancer cells, and FoxP3 for $T_{reg}$ cells). The differentiation between the tumor nest and stroma, as well as the area calculations, were performed based on the pan-cytokeratin staining patterns by utilizing an algorithm integrated into the inForm software. The integrated matrix

files were derived from the segmentation of the cells and tissues from the TMA data. These data included the fluorescence intensity in the nucleus and cytosol. The extracted CSV file was converted into an FCS file using the R software. The FCS file was subsequently converted to a raw file for cytometric image analysis using FlowJo (version 10.9.0).

## 2.18 MoA analysis of CJRB-101

### 2.18.1 Isolation of cell membrane fraction

The bacterial pellet was resuspended in 0.1 M sodium citrate buffer (pH 4.7) and disrupted by ultrasonication (Vibracell VCX500; Sonics and Materials, Newtown, CT) with stirring on ice for 90 min. The bacterial lysates were mixed with an equal volume of n-butanol and the aqueous phase (lower phase) was collected by centrifugation at 13,000 × g for 15 min. The collected aqueous phase was dialyzed using a dialysis membrane (Spectrum Laboratories, Rancho Dominguez, CA) against sterile water (Daihan Pharm. Co. Ltd., Seoul, Korea) at 4 ℃ for 72 h, with sterile water three times a day. The cell membrane fraction was lyophilized and the quantity was determined by measuring the dry weight.

### 2.18.2 Isolation of cell wall fraction

The bacterial pellet was resuspended in 1 M NaCl in phosphate-buffered saline (PBS) and homogenized seven times with glass beads for 1 min each using a bead beater (Biospec Products, Bartlesville, OK, USA) at 4 ℃. The bacterial lysates were taken from the supernatant after removing the glass beads by centrifugation at 2,000 × g for 10 min at room temperature. After collecting the bacterial lysates, the crude cell wall fraction was recovered from the supernatant by centrifugation at 13,000 × g for 10 min, followed by incubation with 0.5% sodium dodecyl sulfate in PBS at 60 ℃ for 30 min. The crude cell wall fraction was resuspended in 1 M Tris–HCl (pH 7.0) and treated with DNase I and RNase A at 37 ℃ for 2 h and then with trypsin containing 10 mM $CaCl_2$ in 1 M Tris–HCl (pH 7.0) at 37 ℃ for 18 h to remove nucleic acids and proteins, respectively. After washing ten times with sterile distilled water, the cell wall fraction was lyophilized and the quantity was determined by measuring the dry weight.

### 2.18.3 Isolation and differentiation of BMDM

Bone marrow was isolated from the mouse (C57BL/6N Female) tibia and femur bone. The

major muscles around the tibia, femur bone, and joints were cut. The bone marrow was flushed using a 25G needle and a 10 mL syringe with RPMI (10% FBS, 1% anti-anti). Bone marrow cells were centrifuged at 1500 RPM for 3 min at room temperature. The supernatant was discarded, and the cells were resuspended in 2 mL of 1x RBC lysis buffer and incubated for 2 min at room temperature. Adding 18 mL RPMI (10% FBS, 1% anti-anti) was added to the bone marrow and centrifuged at 1500 RPM for 3 min at room temperature. The bone marrow cells were resuspended in 10 mL RPMI (10% FBS, 1% anti-anti) and passed through a 100-μm cell strainer. Using a Countess II Automated Cell Counter (Thermo Fisher Scientific, Waltham, MA, USA), 8 x $10^6$/petri dish bone marrow cells were cultured in 10 mL RPMI (10% FBS, 1% anti-anti) supplemented with 10 ng/mL M-CSF (315-02, Peprotech New Jersey). After 4 days, the culture medium was replaced with fresh RPMI (10% FBS, 1% anti-anti, 10 ng/mL M-CSF), and bone marrow cells were incubated for an 3 additional days.

### 2.18.4 Repolarization assay

After differentiation of bone marrow-derived macrophages, the cells were seeded in 24-well plates (1 x $10^5$/well) and incubated for 1 d at 37 °C in a 5% CO2 incubator. For BMDM polarization and repolarization assays, culture media were replaced with RPMI (10% FBS, 1% anti-anti, 10 ng/mL M-CSF) and treated with 100 nM dexamethasone (D9184, Sigma) for 1 day at 37ºC, 5% $CO_2$. For the CJRB-101 efficacy test, CJRB-101 were treated with BMDMs (BMDM to bacteria ratio 1:10) for 1 day at 37ºC, 5% $CO_2$. To confirm the effectiveness of CJRB-101, fractionated CJRB-101, CJRB-101 cell wall (100 μg/mL), and CJRB-101 cell membrane (100 μg/mL) were treated with BMDMs for 1 day at 37ºC, 5% $CO_2$. For the TLR4 antagonist test, cells were pre-treated with the TLR4 antagonist TAK-242 (S7455, Selleckchem) for 1 h before treatment with CJRB-101 and incubated for 1 day at 37ºC, 5% $CO_2$. In this study, flow cytometry was used to analyze the populations of M1 and M2 macrophages. BMDMs were collected using EDTA buffer (PBS containing 1 mM EDTA and 2% FBS) and washed with 1 mL FACS buffer (PBS containing 2% FBS). For M1 and M2 macrophages, BMDM were stained with anti-mouse EMR1 (565410; BD Biosciences), anti-mouse IA-IE (563413; BD Biosciences), and anti-mouse CD206 (565250; BD Biosciences).

## 2.19 Co-culture viability test

### 2.19.1 Isolation of CT26 TAM

CT26 subcutaneous tumor tissues were harvested and placed in enzyme buffer (RPMI, 2% FBS, 0.01 mg/mL DNase I (10104159001, Roche) and 400 U/mL Collagenase IV (LS004139, Worthington). Tumor tissues were cut into small pieces using scissors and dissociated into single-cell suspensions using gentleMACS with agitation for 1 hour at 37ºC. Samples were filtered using a 70-μm cell strainer and washed with FACS buffer (PBS, 2% FBS, 10 mM EDTA, 1% antibiotic-antimycotic, and 10 mM HEPES (H0887, Sigma] ). A single-cell suspension was incubated with RBC lysis buffer for 2 min at room temperature and washed with FACS buffer. $F4/80^+$ cells were isolated by MACS using mouse anti-F4/80 MicroBeads (130-110-443; Miltenyi, Germany) in accordance with the manufacturer's instructions.

### 2.19.2 Isolation of $CD8^+$ $T_c$ cells from Splenocytes

Mouse splenocytes were obtained from C57BL/6 mice. The spleen was flushed using a 25G needle in HBSS (14175-095, Gibco) with collagenase IV (17104-019, Gibco) and incubated for 25 min at 37 °C in a 5% $CO_2$ incubator. 1 mM EDTA (AM9260G, Invitrogen) was added and the mixture was incubated for 5 min at 37 °C in a 5% $CO_2$ incubator. The cells were then centrifuged at 1500 RPM for 3 min at room temperature. To lyse RBC, a single-cell suspension was incubated with RBC lysis buffer for 2 min at room temperature and washed with FACS buffer. $CD8^+$ $T_c$ cells were sorted using a naive $CD8^+$ T-cell isolation kit (130-093-244, Miltenyi, Germany) by MACS in accordance with the manufacturer's instructions.

### 2.19.3 Cytotoxicity against cancer cells and measurement of CXCL9

$CD8^+$ $T_c$ cells, TAMs, and CT26 cancer cells were co-cultured using a Transwell system. In the bottom of 24-well plates pre-coated with 0.1 μg/ml anti-CD3, 1 x $10^4$ CT26 cancer cells and $CD8^+$ $T_c$ cells were seeded and supplemented with 1 μg/ml soluble anti-CD28, 30 U/ml mIL-2, and 10 ng/ml IFNγ. Sorted TAMs were placed in 0.4 μm transwell inserts at a density of 5 × $10^4$ cells/insert and treated with 100 μg/ml CJRB-101 CM Fraction and 10 ng/ml M-CSF.

The co-culture ratio of cancer cells, TAMs, and T-cells was maintained at 1:5:25. After a 1-day incubation, the culture medium was harvested for measurement of mouse CXCL9 (558341, BD). Following a 2-day incubation period, cancer cell viability was assessed using a Fixable Viability

Stain 510 Dye by FACS analysis.

### 2.19.4 T cell activation with TAM and CM fraction

Splenocyte and TAMs co-cultures were conducted using the transwell system. Splenocytes were seeded at a density of 2.5 x $10^5$ cells/well in the bottom of 24-well plates pre-coated with 0.1 μg/mL anti-CD3 and supplemented with 1 μg/mL soluble anti-CD28, 10 ng/ml M-CSF, and 30 U/mL mIL-2 (210-12, Peprotech). Sorted TAMs were placed in 0.4 μm transwell inserts (3413, Corning) at a density of 5 × $10^4$ cells/insert and treated with 100 μg/mL CJRB-101 CM fraction. The TAMs to splenocytes co-culture ratio was 1:5. After 2 days of incubation, splenocytes were collected, and the activated $CD8^+$ $T_c$ cell population was measured by FACS analysis.

## 2.20 Statistical analysis

Data are reported as mean ± SEM. All statistical calculations were performed using Prism 9.0 (Graph Pad Software Inc., USA) and R software. Statistical analysis of the flow cytometry data was performed using the t-test in GraphPad Prism. Significant differences were evaluated using unpaired samples t-test and one-way analysis of variance (ANOVA). Statistical p-value less <0.05.

# 3. Results

## 3.1 Gut microbiome is associated with response to pembrolizumab in advanced NSCLC

A total of 49 patients diagnosed with advanced NSCLC and treated with pembrolizumab monotherapy or in combination with chemotherapy were analyzed to identify metagenomic biomarkers (Fig. 1A). Baseline tumor tissue samples for whole-exome sequencing (WES) (n=40) and RNA sequencing (n=47), baseline and cycle 2 d 1 (C2D1) sampling for metagenome sequencing (baseline and C2D1, n=49), and PBMC and plasma sampling (baseline and C2D1, n=49) were prospectively analyzed. Adenocarcinoma and squamous cell carcinoma comprised 73% (n=36) and 27% (n=13) of the cases, respectively (Supplementary Table S1). Seventeen patients with high PD-L1 expression (PD-L1≥50%) were treated with pembrolizumab monotherapy. Pembrolizumab plus chemotherapy was administered to 32 patients (PD-L1<1%, n=8; PD-L1 1 –49%, n=20; PD-L1≥50%, n=4). Clinical response was observed in 14 patients (29%), including five patients in the pembrolizumab group and nine patients in the pembrolizumab plus chemotherapy group. A chest computed tomography (CT) scan showed a favorable response to pembrolizumab and maintenance of partial response at 9 months (Fig. 1B).

TPS was not significantly different between responders and non-responders (Fig. 1C), and tumor mutation burden (TMB), calculated from the WES data, also showed no significant difference between the two groups. Gene set enrichment analysis (GSEA) revealed that immune-related gene sets, such as the intestinal immune network for IgA production, antigen processing and presentation, graft versus host disease, cytokine-cytokine receptor interaction, JAK-STAT signaling pathway, and $F_c$ gamma receptor-mediated phagocytosis, were higher in the TME of the responder group than in that of the non-responder group (Fig. 1C). In the cytokine assay, we compared 28 features at each sampling point, with interleukin-4 (IL-4) showing higher levels in non-responders during screening ($p$<0.05). In PBMC, a total of 25 features were compared at each sampling point, with four features that were significantly different at screening: HLA-DR$^+$CD68$^+$ ($p$<0.001), CD4$^+$TIM3$^+$ ($p$<0.05), CD4$^+$ ($p$<0.05), and CD3$^+$CD4$^+$($p$<0.05). Two features significantly differed after cycle 2, day 1, HLA-DR$^+$CD68$^+$ ($p$<0.01), and Classical DC featuring CD11c$^+$HLA-DR$^{high+}$ ($p$<0.05, Supplementary). In the analysis of taxonomic features from metagenome sequencing, we compared

366 taxa at screening and 403 taxa after cycle 2 and day 1 using LEfSe. Eight and 17 taxa were identified as taxonomic markers between the two groups at each sampling point (Supplementary Fig. S1A and S1B). We compared the significance of the features found in each analysis using the area under the curve (AUC) values calculated from Wilcoxon rank-sum test statistics (Fig. 1D). Instead of TPS or TMB, AUC values differentiated responders from non-responders, indicating that the response to pembrolizumab is associated with host-driven features, as well as the gut microbiome.

To further explore this relationship, we analyzed the metagenome sequencing data and found no statistically significant differences in microbial diversity between responders and non-responders (Fig. 1E). Furthermore, no clear distinction was observed in the principal coordinate analysis plot (Fig. 1F). We assumed that the response to pembrolizumab could be influenced by multiple factors, potentially hindering a clear distinction between responders and non-responders, based solely on the composition of the gut microbiome. Therefore, we classified the fecal samples according to enterotype (Fig. 1G). As a result, two enterotypes were identified, characterized by high-diversity enterotype 2 (E2, 133.0 ± 29.7 number of species with 3.7 ± 0.4 Shannon index) and low-diversity enterotype 1 (E1, 73.7 ± 27.0 with 2.7 ± 0.8 Fig. 1H). Members of *Bacteroidaceae* and *Oscillospiraceae* were significantly more abundant in E2 ($p<0.01$, and $p<0.0001$, respectively; Supplementary Fig. S1C). We observed that the samples derived from responders were significantly more prevalent in E2 (70.2% vs. 48.4%, $p<0.05$, Fig. 1I), highlighting the relationship between response to pembrolizumab and the gut microbiome.

| Characteristics | All (N=49) | Pembrolizumab (N=17) | Pembrolizumab plus chemotherapy (N=32) |
|---|---|---|---|
| **Age** | | | |
| Median (range), year | 66 (40-87) | 69 (47-87) | 64 (40-85) |
| **Sex** | | | |
| Male | 43 (88) | 16 (94) | 27 (84) |
| Female | 6 (12) | 1 (6) | 5 (16) |
| **ECOG performance-status** | | | |
| 0 | 5 (10) | 1 (6) | 4 (13) |
| 1 | 44 (90) | 16 (94) | 28 (87) |
| **Smoking status** | | | |
| Current or former | 43 (88) | 16 (94) | 27 (84) |
| Never | 6 (12) | 1 (6) | 5 (16) |
| **Histologic features** | | | |
| Adenocarcinoma | 36 (73) | 14 (82) | 22 (69) |
| Squamous cell carcinoma | 13 (27) | 3 (18) | 10 (31) |
| **Brain metastasis** | | | |
| Yes | 25 (51) | 6 (35) | 19 (59) |
| No | 24 (49) | 11 (65) | 13 (41) |
| **PD-L1 by TPS** | | | |
| <1% | 8 (16) | 0 (0) | 8 (25) |
| 1-49% | 20 (41) | 0 (0) | 20 (63) |
| >50% | 21 (43) | 17 (100) | 4 (12) |
| **Clinical response** | | | |
| Responder* | 14 (29) | 5 (29) | 9 (28) |
| Non-responder** | 35 (71) | 12 (71) | 23 (72) |

**Supplementary Table S1. Baseline characteristics of the CJ microbiome cohort (N=49).** **Abbreviations**: ECOG, Eastern Cooperative Oncology Group; PD-L1, programmed death-ligand 1; TPS, tumor proportion score. ECOG, Eastern Cooperative Oncology Group; PD-L1, programmed death-ligand 1; TPS, tumor proportion score. **Non-responder defined as SD of less than 6 months and progressive disease.

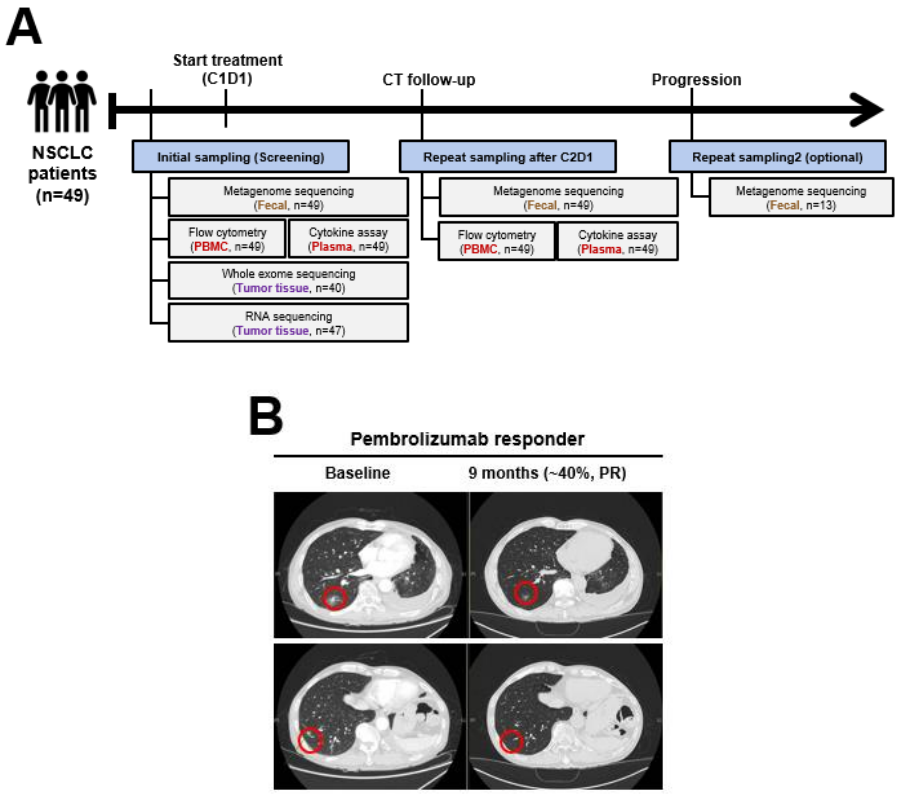


**Figure 1.** Data analysis for the pembrolizumab treated advanced NSCLC patients. **A)** Schematic overview of sample collection for pembrolizumab treated advanced NSCLC patients (n=49). **B)** Lung CT scan images of a responder, taken before and after the treatment. Tumor response was assessed with Response Evaluation Criteria in Solid Tumor version 1.1 (RECIST v 1.1).

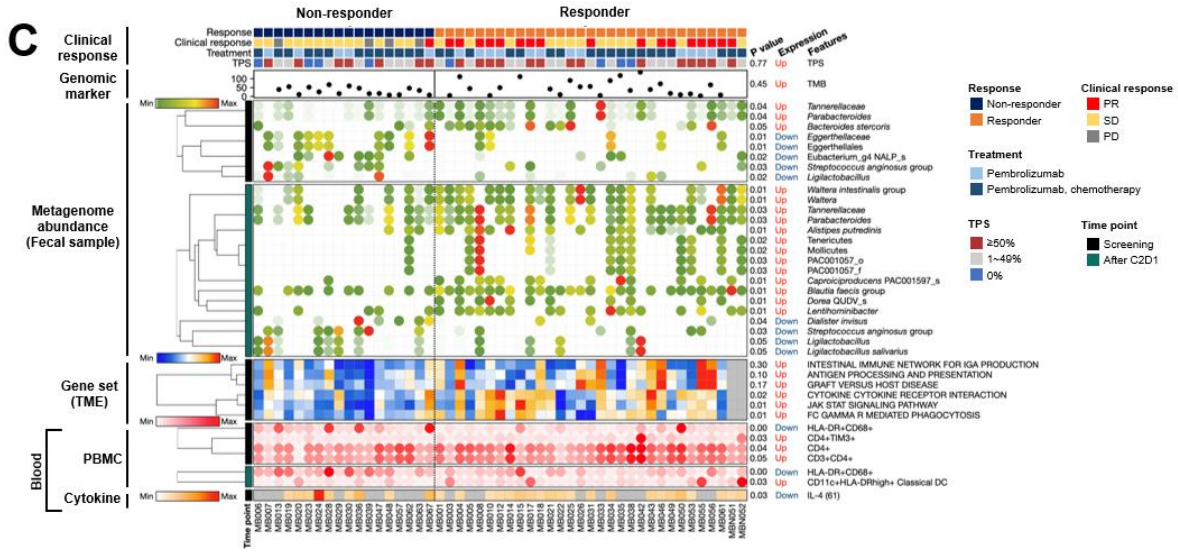


**Figure 1C)** Significantly different features in RNA sequencing, cytokine assay, flow cytometry and metagenome sequencing between responders and non-responders. *P-values* were plotted on the right side. Responder-enriched features were labeled as 'Up' and non-responder-enriched features were labeled as 'Down'. The average expression of genes was displayed.

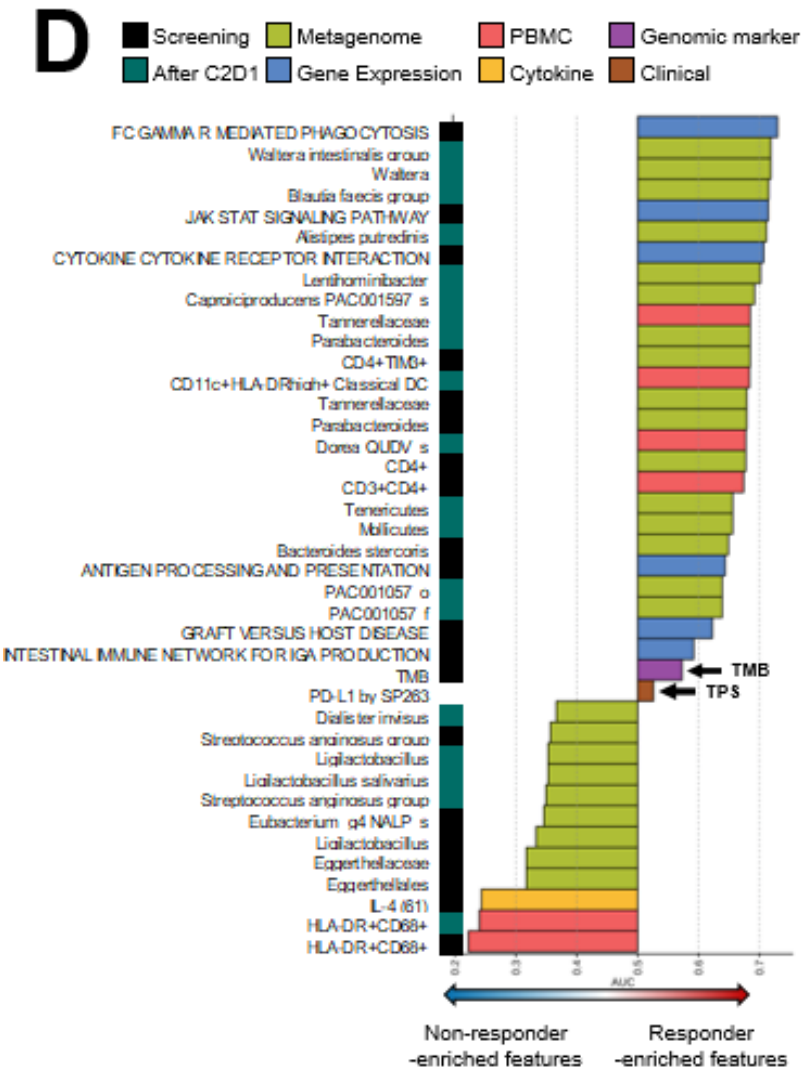


**Figure 1D)** Area under the curve (AUC) values from Figure 1C were plotted.

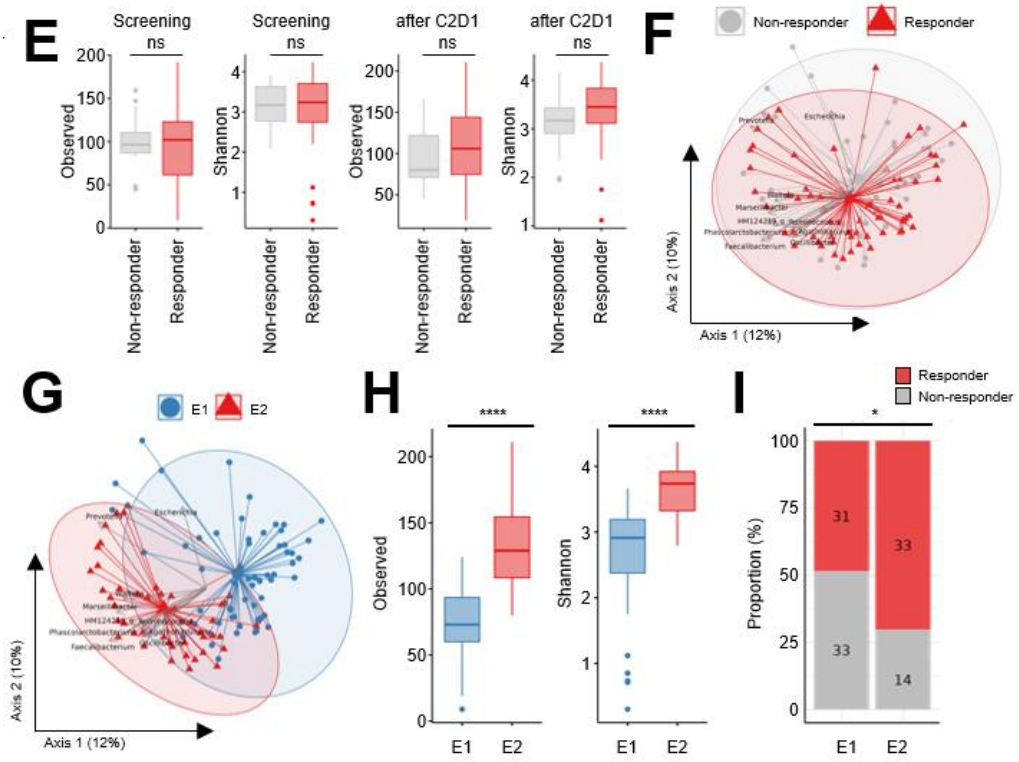


**Figure 1E)** Alpha diversity indices, including the number of observed species and the Shannon index, were compared between responders and non-responders at the baseline and after cycle 2, day1 using the rarefied number of reads (6,588 reads per sample, Wilcoxon rank sum test). Principal coordinate analysis (PCoA) plots of Bray–Curtis distances at the genus level were generated using the rarefied number of reads (6,588 reads per sample) and colored by response information **(F)** and enterotypes **(G)**. **H)** Alpha diversity indices, including the number of observed species and the Shannon index, were compared between E1 and E2 using the rarefied number of reads (6,588 reads per sample, Wilcoxon rank sum test). **I)** Proportions of responder-derived and non-responder-derived samples in each enterotype. *P-values* were calculated by the Fisher-exact test. ns: $p > 0.05$, *: $p \leq 0.05$, **: $p \leq 0.01$, ***: $p \leq 0.001$, ****: $p \leq 0.0001$.

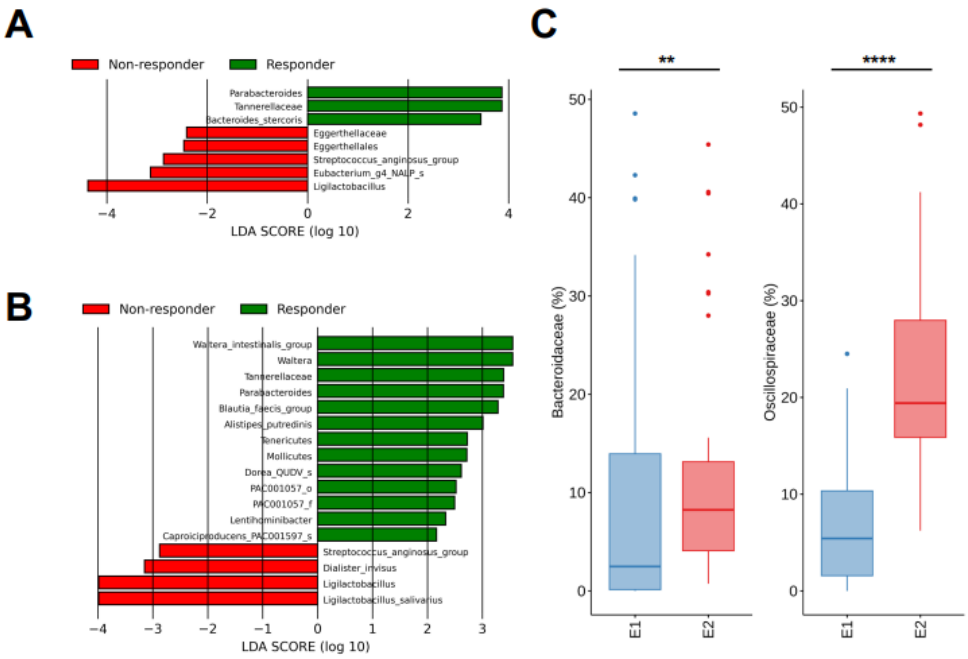


**Supplementary Figure S1. Differences in microbial features between responders and non-responders and between enterotype 1 (E1) and enterotype 2 (E2).** Differentially abundant taxa between responders and non-responders at the screening **(A)** and after cycle 2, day 1. **B)** Features were filtered based on a 20% prevalence, and unassigned features were excluded. LEfSe was used for taxonomic marker discovery. **C)** The abundances of *Bacteroidaceae* and *Oscillospiraceae* were compared between E1 and E2 (Wilcoxon rank sum test). ns: $p > 0.05$, *: $p \leq 0.05$, **: $p \leq 0.01$, ***: $p \leq 0.001$, ****: $p \leq 0.0001$.

## 3.2 CJRB-101 and CJRS-10672 exhibit optimal anti-tumor cytokine profile and efficacy

Probiotic bacterial strains were screened to identify candidate strains that could enhance anti-tumor activity. Using an immune-based screening method, 355 strains were screened, including 140 *Lactobacillus*, 55 *Leuconostoc*, 17 *Pediococcus*, 14 *Weissella*, 52 *Enterococcus*, and 77 *Bifidobacterium* species (Fig. 2A). $Log_2$ fold changes in pro-inflammatory cytokines (IL-6 and IL-1β in mouse macrophages, and IFNγ in mouse splenocytes) at the level of expression and by genus are described in Fig. 2B and 2C, respectively. The proportion of each genus in the highlighted quadrant is shown in Fig. 2D. Including the human macrophage cell line (THP-1), 60 strains were selected, and these strains belonged to *Lactobacillus* (17 strains), *Leuconostoc* (8 strains), *Weissella* (2 strains), *Enterococcus* (24 strains), and *Bifidobacterium* (9 strains, Fig. 2E, Supplementary Fig. S6).

Mouse splenocytes and human PBMCs were co-cultured with 60 strains, and the proportion of $CD8^+IFN\gamma^+$ cells (%) was analyzed using flow cytometry. Four strains (CJRB-101, CJRS-10672, CJRS-17429, and CJRS-17430) with high $CD8^+IFN\gamma^+$ proportions in mouse splenocytes and human PBMC were selected (Fig. 2F). Notably, all four selected strains belonged to *Leuconostoc*. To validate the species of the four strains, we performed genome-based identification and calculated the average nucleotide identity (ANI) value with the type strains of *L. mesenteroides* and *L. citreum* (Supplementary Fig. S8). The ANI value between the type strains of *L. mesenteroides* and CJRB-101 was 99.0%, whereas the ANI value between the type strain and CJRS-10672 was 99.2%. The ANI value between the type strains of *L. citreum* and CJRS-17429 was 99.2%, whereas that between the type strain and CJRS-17430 was 99.1%. Considering that the proposed cut-off for the ANI values for bacterial species is 95–96%(13), we confirmed that CJRB-101 and CJRS-10672 are members of *L. mesenteroides*, and CJRS-17429 and CJRS-17430 are members of *L. citreum* with differing genome sizes and numbers of genes.

The antitumor activity of the four strains was investigated in combination with anti-PD-1 using the LLC1 syngeneic mouse model (Fig. 2G). CJRS-17429 or CJRS-17430 in combination with anti-PD-1 resulted in larger tumor volume at 465.6 $mm^3$ ±78.1 and 726.0 $mm^3$ ±132.7, respectively. Remarkably, CJRB-101 with anti-PD-1 (287.7 $mm^3$ ±59.6) and CJRS-10672 with anti-PD-1 (220.2 $mm^3$ ±65.5) significantly reduced tumor volume compared to the anti-PD1 in LLC1

syngeneic mouse model (663.2 $mm^3$ ±89.7, $p<0.001$ and $p<0.0001$ respectively, Fig. 2G).

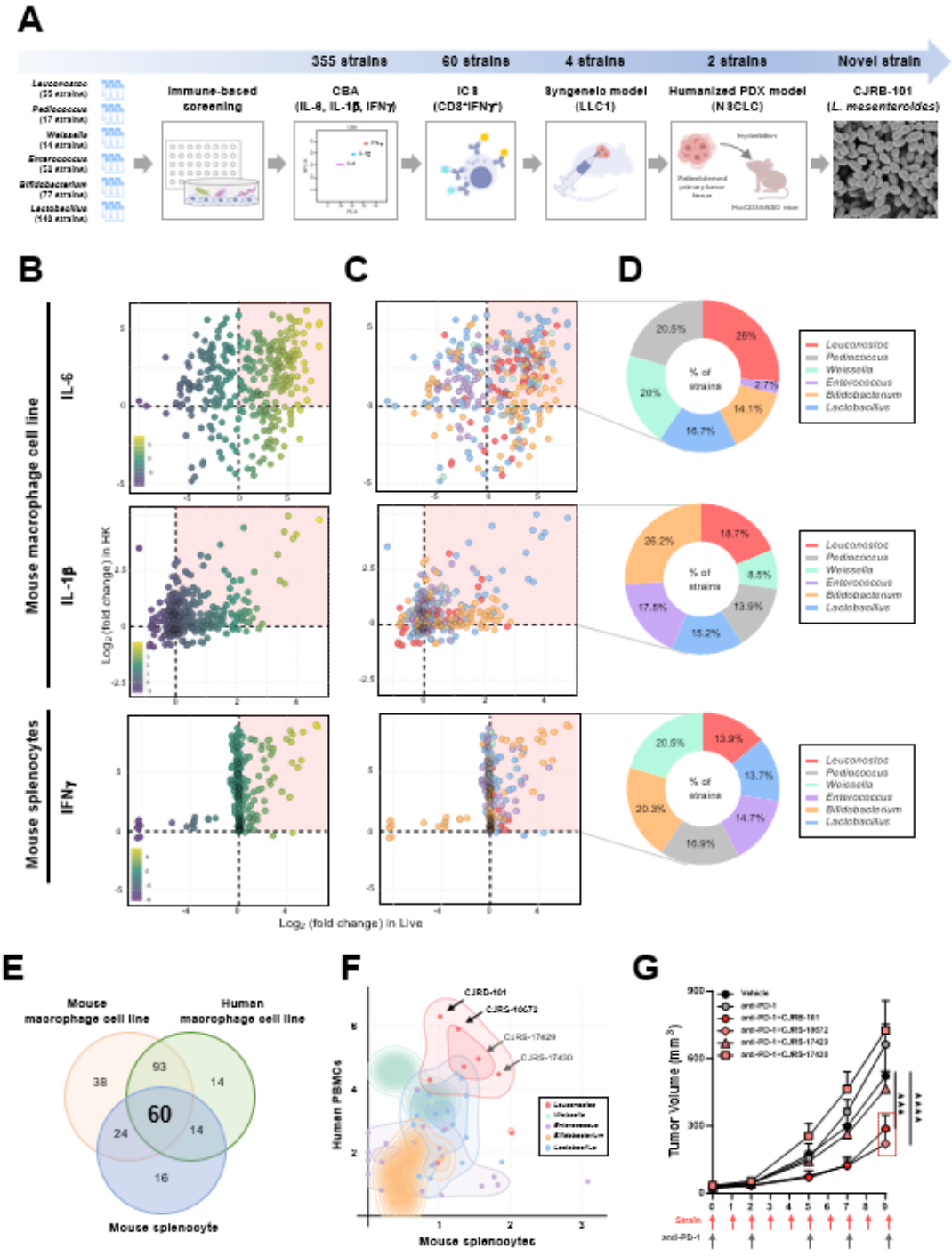

**Figure 2.** Selection of CJRB-101 through immune-based screening tool. **A)** Schematic overview of experiments (in vitro, ex vivo, and in vivo) for the screening. **B, C)** Scatter plot of $log_2$ fold change of cytokines between live strain (X-axis) and heat-killed (HK) strain (Y-axis). Mouse macrophage cell line (Raw264.7) and mouse splenocytes were co-cultured with 355 strains and pro-inflammatory cytokines (IL-6, IL-1β, IFNγ) were measured. $Log_2$ fold change was normalized compared to the amount of cytokine from *Bifidobacterium bifidum*. $Log_2$ fold change was shown by expression level **(B)** and genus **(C)**. **D)** The proportion of genus in highlighted quadrant out of each genus. **E)** Venn diagram displaying the number of bacterial strains induced high cytokine production (IL-6, IL-1β and IFNγ) in Mouse macrophage cell line (Raw264.7 cell) and mouse splenocytes. **F)** The $log_2$ fold change of $IFN\gamma^+$ $CD8^+$ $T_c$ cell in 60 strains co-cultured with human PBMC or mouse splenocytes. The $log_2$ fold change was displayed by genus level. **G)** The top four selected strains (CJRB-101, CJRS-10672, CJRS-17429, and CJRS-17430) were selected and anti-tumor effect was measured using LLC1 syngeneic mouse model.

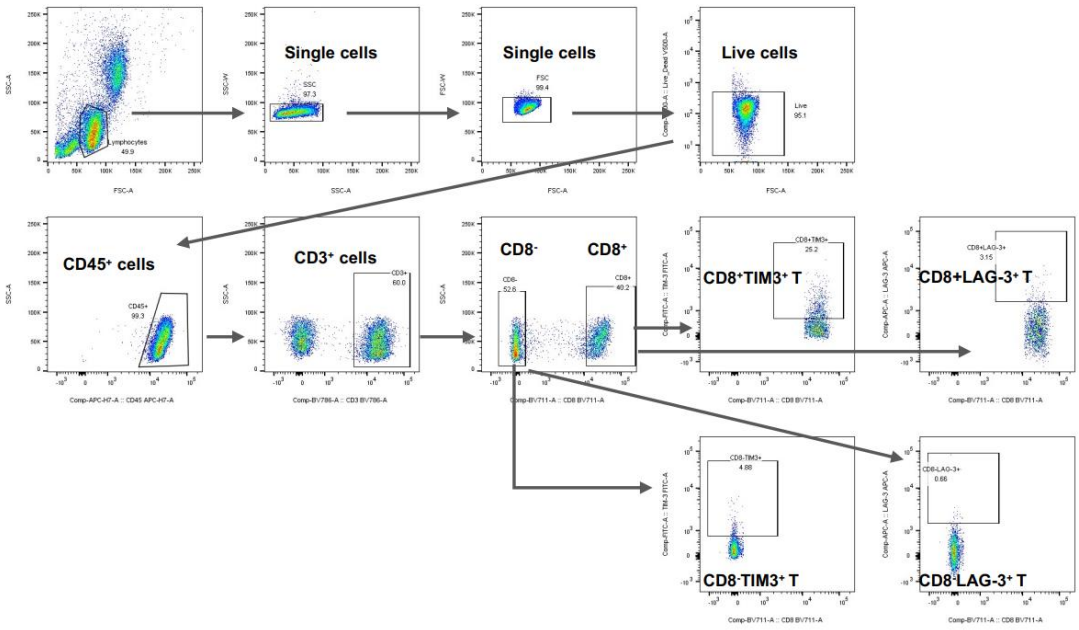


**Supplementary Figure S2. Cohort PBMC gating strategy #1 (T cell panel)**

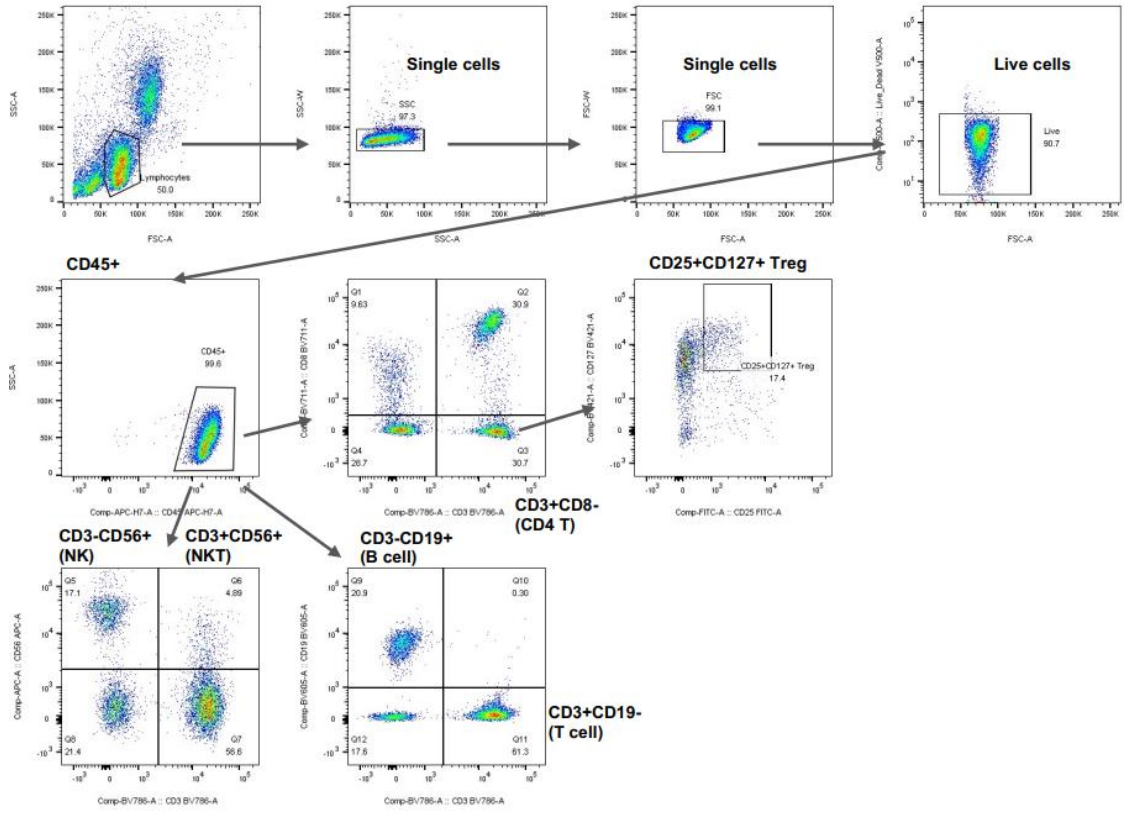


**Supplementary Figure S3. Cohort PBMC gating strategy #2 (NK, T, B cell panel)**

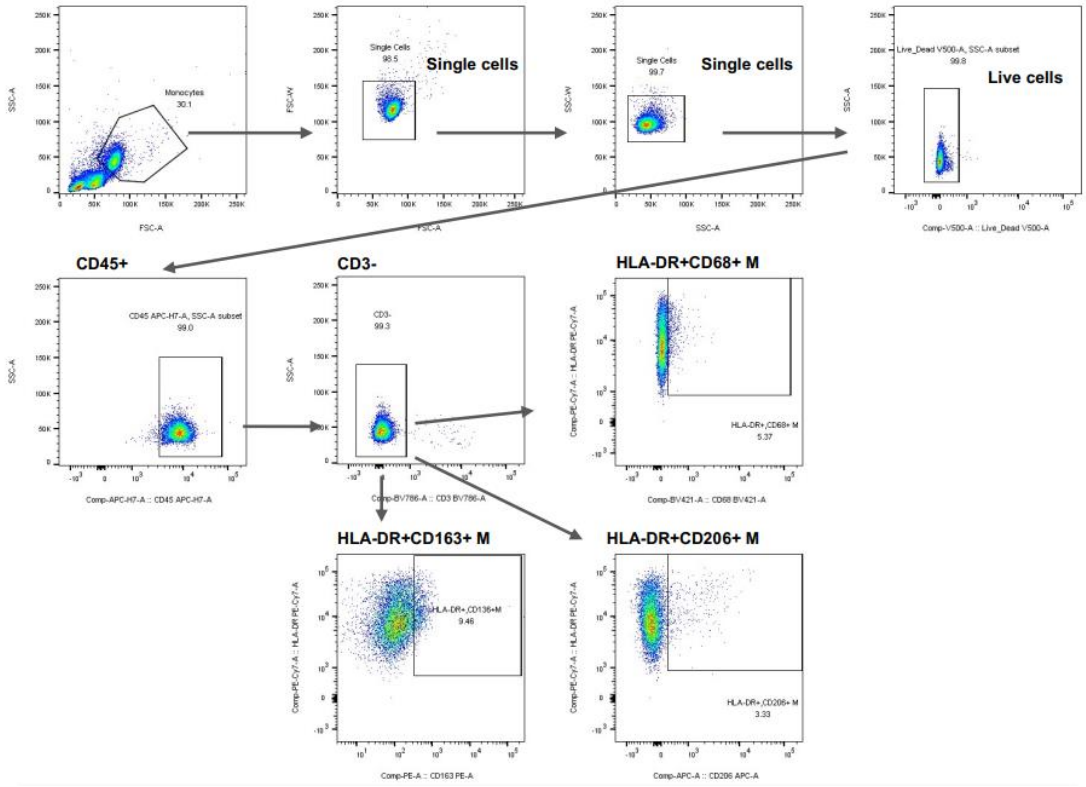


**Supplementary Figure S4. Cohort PBMC gating strategy #3 (Macrophage panel)**

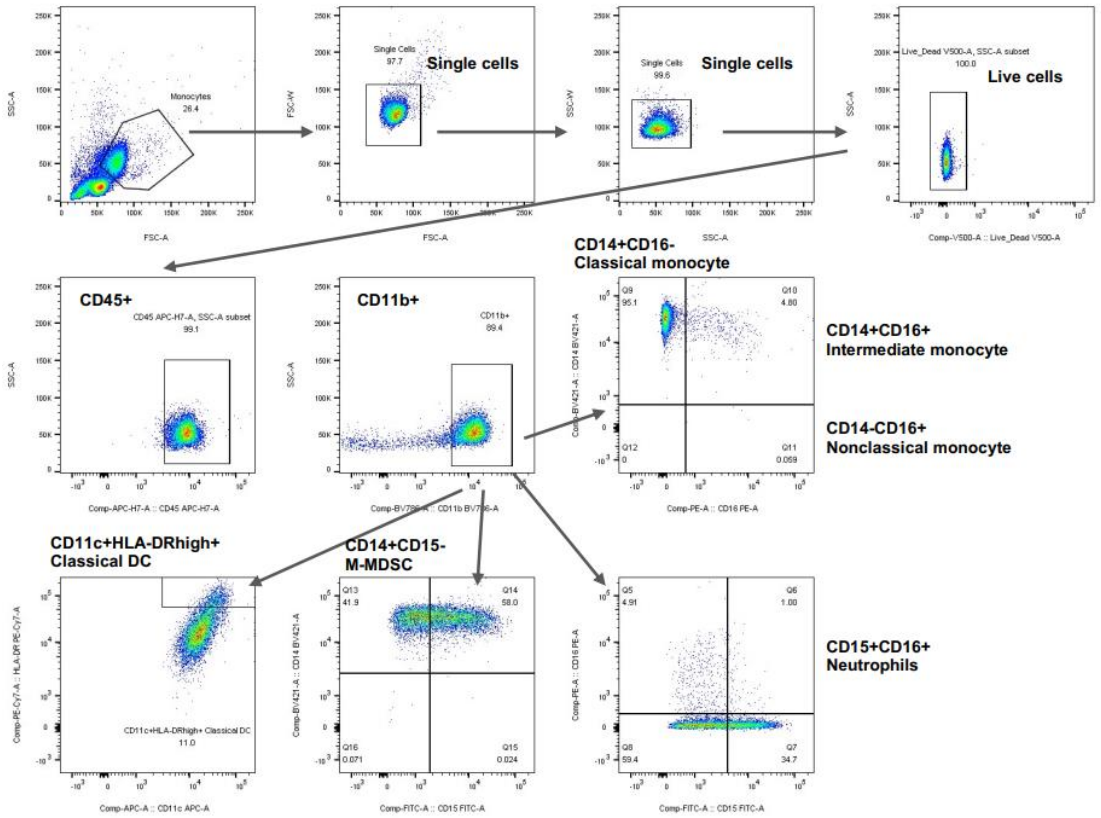


**Supplementary Figure S5. Cohort PBMC gating strategy #4 (Myeloid cell panel).**

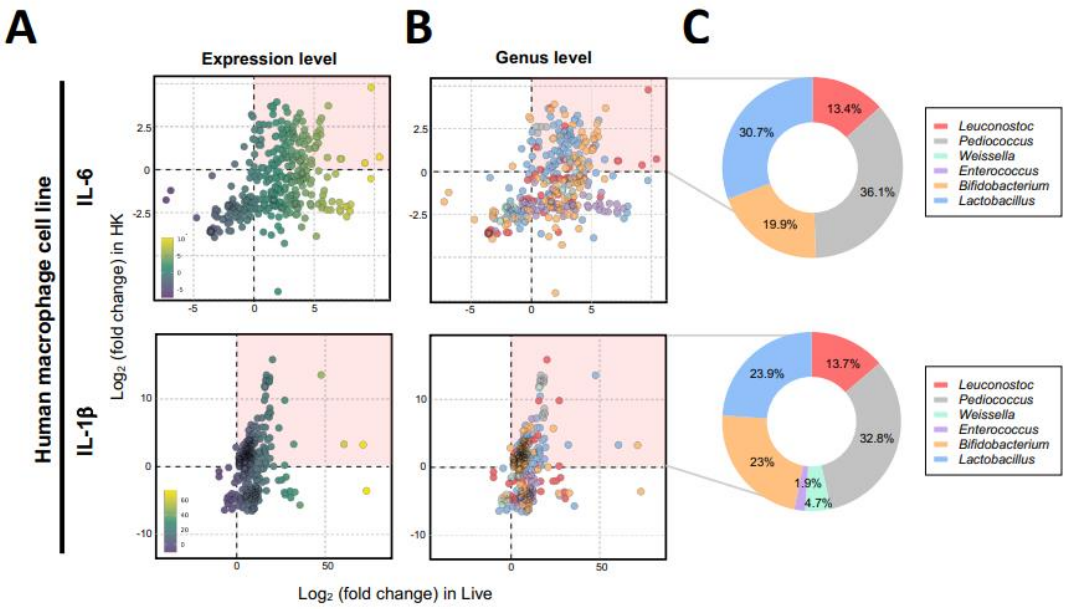


**Supplementary Figure S6. Scatter plot of $log_2$ fold change of cytokines in human macrophage cell line (THP-1).** THP-1 was co-cultured with 355 strains and pro-inflammatory cytokines (IL-6, IL-1β, IFNγ) were measured. $Log_2$ fold change was normalized compared to the amount of cytokine from *Bifidobacterium bifidum*. $Log_2$ fold change was shown by expression level **(A)** and genus **(B)**. **C)** The proportion of genus in highlighted quadrant out of each genus.

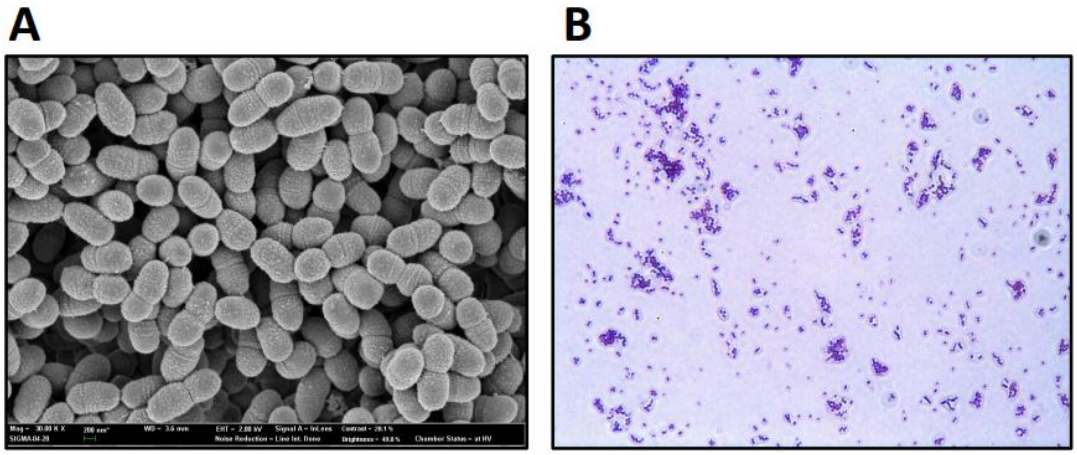


**Supplementary Figure S7. CJRB-101 morphology and gram staining characteristic. A)** Scanning electron microscopy (SEM) images of CJRB-101 (Scale bar = 200 $nm^2$). Small and thin oval-shaped, pair-shaped, or chain-shaped appearance should be observed. **B)** Gram staining under light microscope with magnification 1000x. CJRB-101 is Gram-positive bacteria.

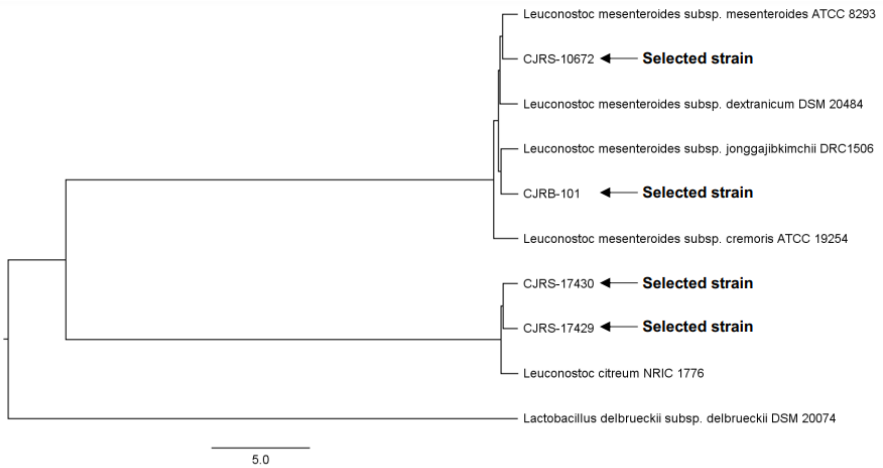


| Strain name | Identified species | Identity | Genome size | GC content | Gene count |
|---|---|---|---|---|---|
| CJRB-101 | *Leuconostoc mesenteroides* | 99.03% | 2,151,929 bp | 37.65% | 2,110 |
| CJRS-10672 | *Leuconostoc mesenteroides* | 99.21% | 2,012,843 bp | 37.57% | 1,970 |
| CJRS-17429 | *Leuconostoc citreum* | 99.19% | 1,969,867 bp | 38.72 % | 1,896 |
| CJRS-17430 | *Leuconostoc citreum* | 99.05% | 2,039,424 bp | 38.64 % | 1,913 |

**Supplementary Figure S8. UPGMA dendrogram based on average nucleotide identity (ANI) values of genomic sequences from CJRB-101, CJRS-10672, CJRS-17429 and CJRS-17430.** The UPGMA dendrogram was generated using nucleotide sequences from the type strains of *Leuconostoc mesenteroides* subspecies, the type strain of *Leuconostoc citreum*, CJRB-101, CJRS-10672, CJRS-17429 and CJRS-17430. *Lactobacillus delbrueckii* subsp. *delbrueckii* DSM 20074$^{T}$ was used as an outgroup. Bar, 5% difference in ANI value. Identity indicates the ANI values against the type strain of identified species. The number of genes in each genome was detected using Prodigal.

### 3.3 CJRB-101 demonstrates immune-driven anti-tumor effects in humanized NSCLC patient-derived xenograft models

A previous study indicated that CJRB-101 and CJRS-10672 stimulated the production of tumor-killing cytokines in human and mouse immune cells, while showing promising antitumor efficacy in the LLC1 syngeneic mouse model. The candidate strains were subsequently tested in humanized patient-derived xenograft (PDX) models with immune profiles and TME similar to those of the human immune system (Supplementary Table S2). Four NSCLC PDX tumors were engrafted into Hu-CD34-NSG mice to generate humanized PDX models (YHIM-2003, YHIM-2004, YHIM-2009, and YHIM-2014; Fig. 3A). These PDX models exhibited primary resistance or insensitivity to pembrolizumab (Fig. 3B). YHIM-2004 PDX cells were treated with CJRB-101 and CJRS-10672 to identify the best candidates. Initial screening showed that CJRB-101 significantly reduced tumor growth compared to CJRS-10672, where the average tumor volume at the end of treatment (EOT) was 399.0 $mm^3$ ±70.8 and 1589.6 $mm^3$ ±122.1, respectively ($p$<0.05, Fig. 3C). Based on these results, CJRB-101 was selected to assess combination treatment with pembrolizumab in humanized NSCLC PDX models. No antitumor effects were observed when immunodeficient NOG mice were treated with CJRB-101, indicating that the immune response of CJRB-101 appears to be driven by immune cells (Fig. 3D). Combination treatment with YHIM-2004 demonstrated that CJRB-101 effectively controlled tumor growth. CJRB-101 alone (722.2 $mm^3$ ±122.6 at EOT) and in combination with pembrolizumab (1398.5 $mm^3$ ±258.9 EOT) significantly reduced tumor volume compared to the vehicle in YHIM-2004 (2442.4 $mm^3$ ±240.1 at EOT, $p$<0.0001 and $p$<0.005, respectively, Fig. 3D).

In YHIM-2009 PDX mice, tumor growth was not controlled by pembrolizumab alone. At EOT, average tumor volume of vehicle and pembrolizumab group was 1240.7 $mm^3$ ±55.8 and 1531.6 $mm^3$ ±99.9 respectively, suggesting that anti-PD-1 immunotherapy appeared to be ineffective in this model (Fig. 3F). However, CJRB-101 in combination with pembrolizumab effectively overcame pembrolizumab resistance by significantly reducing the tumor volume compared to pembrolizumab alone (418.4 $mm^3$ ±14.0, $p$<0.001, Fig. 3F). In the YHIM-2014 and YHIM-2003 PDX models, pembrolizumab alone showed a moderate anti-tumor response (Fig. 3G and 3H, respectively). However, combination treatment significantly reduced tumor growth in YHIM-2014 and YHIM-2003 ($p$<0.001 and $p$<0.01, Fig. 3G and 3H, respectively). At EOT, average tumor volume of the vehicle, pembrolizumab and the combination group was 1823.5 $mm^3$ ±146.6, 855.4 $mm^3$ ±132.3 and 311.9 $mm^3$ ±48.6 respectively in YHIM-2014. In YHIM-2003, average tumor

volumes were 1922.6 $mm^3$ ±83.8, 1346.5 $mm^3$ ±85.2 and 1062.9 $mm^3$ ±74.0, respectively. Specifically, CJRB-101 alone also showed significant anti-tumor efficacy, similar to that of the combination treatment, thereby showing that the anti-tumor response of combination therapy is likely driven by CJRB-101. To investigate the immunomodulatory effects of CJRB-101, changes in the immune cell populations in the TME were examined.

| | YHIM-2003 | YHIM-2004 | YHIM-2009 | YHIM-2014 |
|---|---|---|---|---|
| **Age** | 59 | 77 | 59 | 69 |
| **Sex** | M | M | M | M |
| **Ethnicity** | Korean | Korean | Korean | Korean |
| **Smoking history** | 45PY | 33PY | 40PY | N/A |
| **Histology** | LUSC | LUSC | LUSC | LUSC |
| **EGFR mutation** | WT | WT | WT | WT |
| **Driver mutation (PDX tissue)** | Moderate response | Moderate response | Moderate response | Primary resistance |
| **Durvalumab sensitivity** | **PIK3CA amplification** | **PIK3CA/EGFR amplification** | **PIK3CA amplification** | N/A |
| **HLA-type** | A*31:01 A*11:01 | A*33:01 A*24:02 | A*30:04 A*02:01 | A*33:03 A*32:01 |
| **Stage at diagnosis** | Stage IIB | Stage IB | Stage IIA | Stage IIB |
| **Treatment** | Vinorelbine/ Cisplatin PRAME+Cpg7909 | N/A | Vinorelbine/ Cisplatin | N/A |

**Supplementary Table S2. Information of lung squamous cell carcinoma (LUSC) patient-derived xenograft (PDX) tumors utilized in in vivo efficacy screening of CJRB-101.** PY = pack year, (cigarettes per day/pack size) x years; WT = wild type; N/A = not accessible; HLA = human leukocyte antigen.

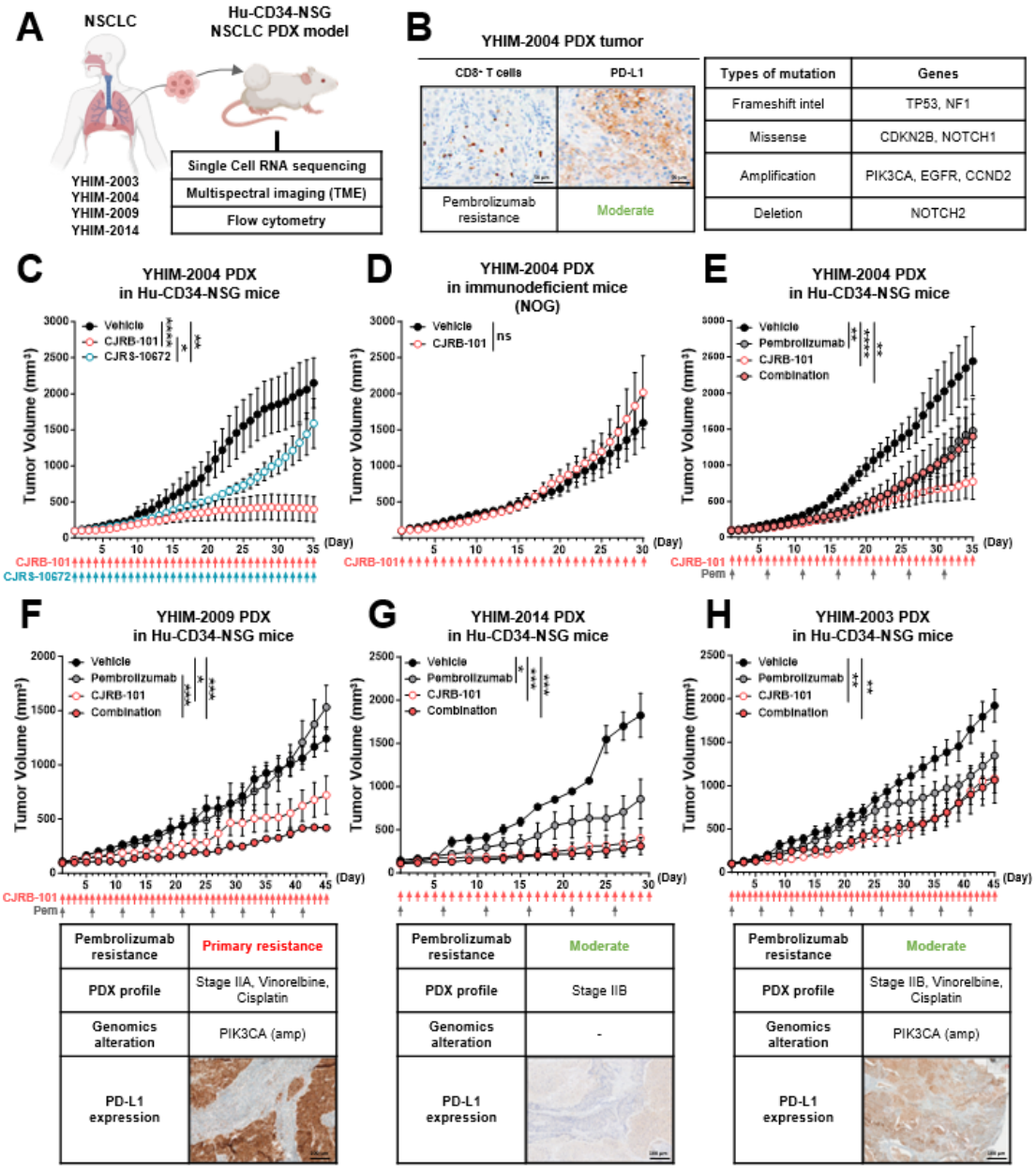


**Figure 3.** CJRB-101 and pembrolizumab combination treatment demonstrated significant anti-tumor efficacy in humanized non-small cell lung cancer (NSCLC) PDX models. **A)** Schematic design and analysis of humanized YHIM-2003, YHIM-2004, YHIM-2009 and YHIM-2014 PDX

models. **B)** Level of $CD8^+$ $T_c$ cells and PD-L1, and the mutation profile of YHIM-2004 PDX tumor. **C)** Humanized PDX mice bearing YHIM-2004 tumor treated with CJRB-101 and CJRS-10672, showing significant tumor reduction by CJRB-101 in comparison to CJRS-10672 ($p<0.05$). **D)** Tumor progression of YHIM-2004 PDX treated with CJRB-101 in immunodeficient NOG mice, demonstrating that the immune response of CJRB-101 is immune cell-mediated. **E)** Combination treatment of CJRB-101 and pembrolizumab in YHIM-2004 PDX model, showing significant tumor reduction by CJRB-101 alone and in combination. **F)** Combination treatment of CJRB-101 and pembrolizumab (top) and mutation profile (bottom) of YHIM-2009 PDX model. Combination treatment significant reduced tumor volume compared to pembrolizumab alone ($p<0.001$), demonstrating that combination treatment overcame resistance to pembrolizumab. **G)** Combination treatment of CJRB-101 and pembrolizumab (top) and mutation profile (bottom) of YHIM-2014 PDX model. CJRB-101 alone showed similar anti-tumor effects to the combination treatment in YHIM-2014 PDX. **H)** Combination treatment of CJRB-101 and pembrolizumab (top) and mutation profile (bottom) of YHIM-2003 PDX model.

### 3.4 CJRB-101 induces macrophages expressing T cell chemoattractants in the tumor microenvironment

Previous assays have shown that CJRB-101 stimulates cytokine production in macrophages and that the anti-tumor responses of CJRB-101 are driven by immune cells (Fig. 3D and 3E). Thus, the tumor of the YHIM-2004 PDX was examined to compare changes in the subsets of macrophages. Immune profiling of myeloid lineage cells demonstrated that the combination treatment induced a higher ratio of M1 to M2 macrophages, indicating that the combination treatment generated a population shift towards an immune-boosting phenotype in the macrophages within the tumor (Fig. 4A). The M1/M2 ratio was significantly higher in the combination group (0.7 ±0.1) than in the vehicle (0.4 ±0.1, $p<0.01$) and pembrolizumab-treated group (0.5 ±0.1, $p<0.01$, Fig. 4A). Combination treatment resulted in higher expression of activation markers such as CD80 in M1 macrophages, significantly increasing the level of CD80 in the combination group (1496.5 ±92.8) compared to vehicle (984.8 ±244.7, $p<0.01$) and pembrolizumab (1238.4 ± 170.0, $p<0.05$, Fig. 4B). The immunomodulatory effects of combination treatment were also evident in the TME. Indicative markers of monocytes and macrophages in the TME were examined to investigate the role of myeloid cells in immunoediting in the TME. Figure 4C demonstrates that macrophages were detected in the tumor across the treatment groups and that PD-L1 increased in the CJRB-101 treated group, providing a rationale for the combination treatment of CJRB-101 with anti-PD-1 immunotherapy. The average cell count of macrophages in the TME was significantly higher in the pembrolizumab group than in the other groups (Fig. 4D). Interestingly, M1 macrophages ($CD68^{+}CD11c^{+}$) were significantly increased in the combination group (56.8) compared to those in the vehicle ($p<0.0001$, 9.2), pembrolizumab ($p<0.0001$, 12.5), and CJRB-101 ($p<0.05$, 35.4) groups (Fig. 4D). CJRB-101 and pembrolizumab enhanced the proportion of immune-favorable M1 macrophages in the TME and contributed to the effective control of tumor cell growth.

We identified 11 clusters, each characterized by distinct cluster marker genes via single-cell RNA sequencing (scRNA-seq) analysis (Supplementary Fig. S12 and S13). We extracted C1_Macro/Mono/DC clusters for further analysis. After additional filtering for macrophages and monocytes, we identified subclusters within this group and 11 clusters characterized by unique markers (Fig. 4E, Supplementary Fig. S14). We identified the top 10 genes in the treatment groups (Fig. 4F). The C1_Macrophage and C5_Macrophage clusters showed higher expression of the top genes in CJRB-101 treated group (Fig. 4G, Fig. 4H). The C1_Monocyte cluster predominantly

expressed marker genes that were enriched in both the vehicle and pembrolizumab groups, whereas the C7_Macrophage cluster exhibited higher expression of marker genes specifically associated with the pembrolizumab group (Fig. 4G, Fig. 4H). The C7_Macrophage cluster was closer to monocytes than the C1_Macrophage and C5_Macrophage clusters, which were enriched in CJRB-101. Thus, CJRB-101 may contribute to the progressive development of macrophages compared with pembrolizumab alone (Fig. 4H). We then compared the abundance of enriched macrophage clusters in CJRB-101 treated group (C1_ and C5_Macrophage clusters) and the pembrolizumab group (C7_Macrophage cluster, Fig. 4I). The proportion of enriched macrophage clusters in the CJRB-101-treated group was significantly higher than that in the pembrolizumab group ($p<0.05$). Gene expression analysis of enriched macrophage clusters in both groups demonstrated that the macrophage clusters enriched in the CJRB-101-treated group showed elevated expression of CXCL10 and CCL2, which are chemoattractants of T cells (Fig. 4J and Supplementary Fig. S15),

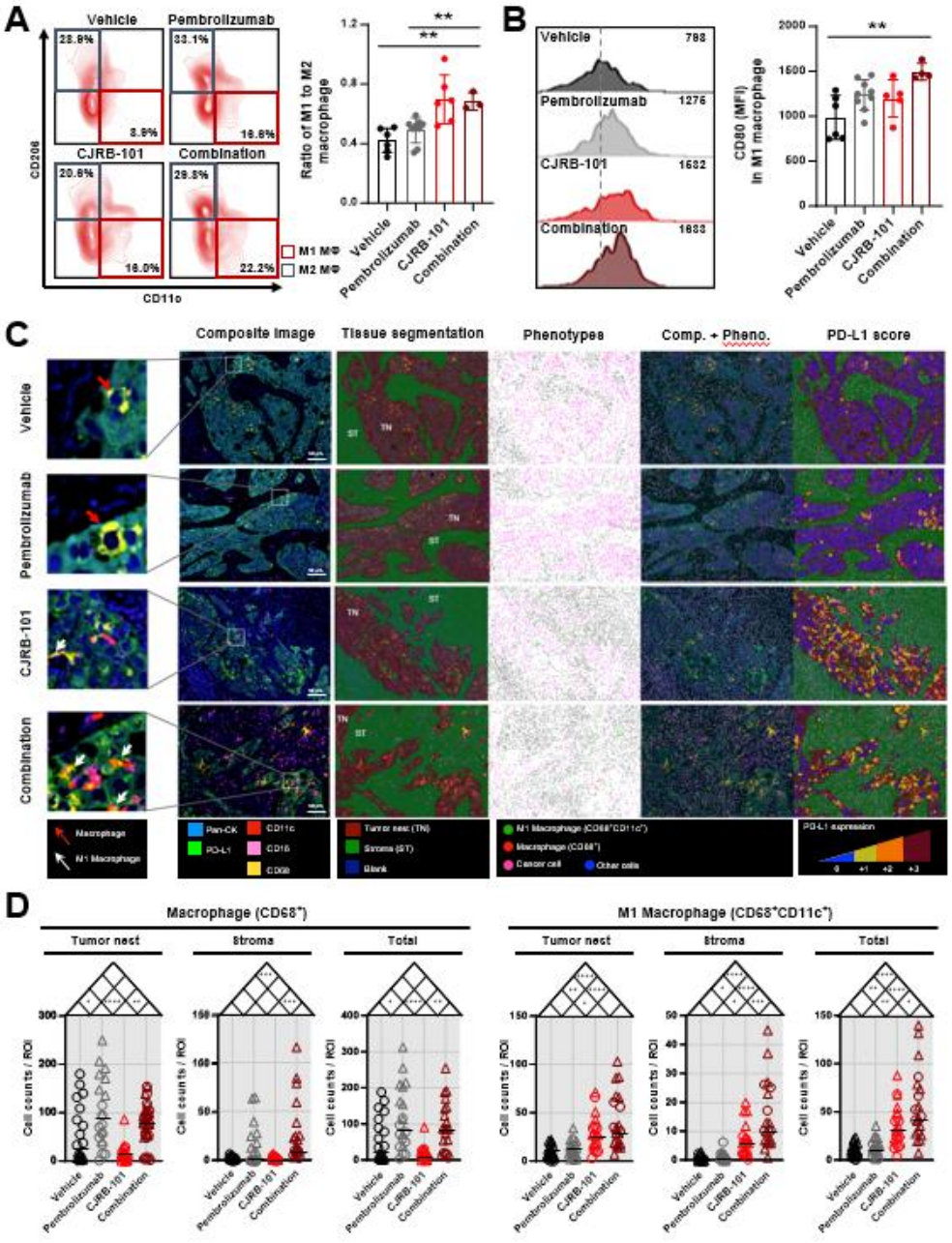

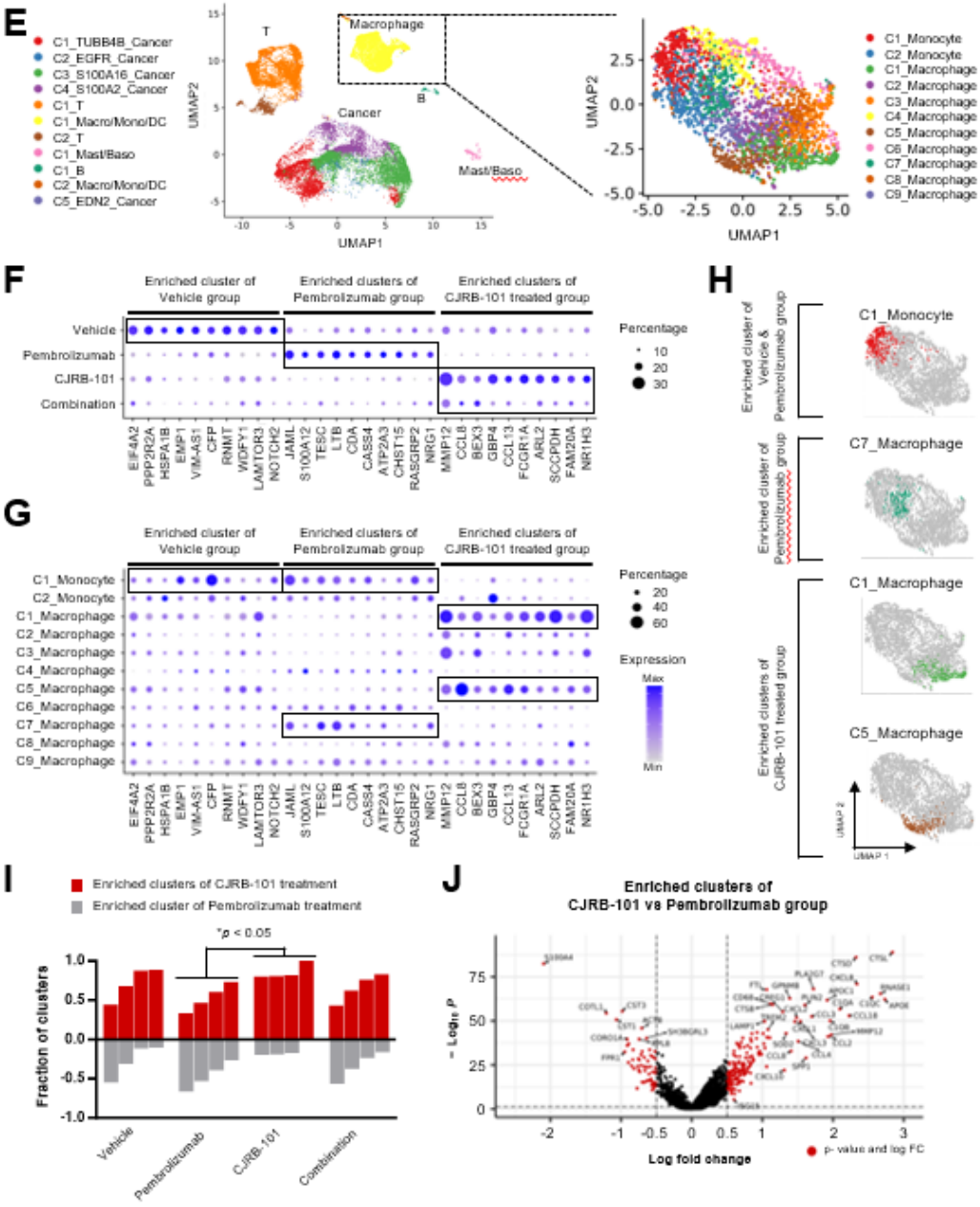

**Figure 4**. Myeloid cell-mediated anti-tumor effects of CJRB-101 in combination treatment of humanized NSCLC YHIM-2004 PDX model. **A)** Proportional changes in macrophage subtypes (M1 and M2) by combination treatment of CJRB-101 and pembrolizumab in humanized YHIM-2004 PDX tumor, showing significantly increased ratio of M1 to M2 macrophages by combination treatment compared to pembrolizumab treated group ($p$<0.01). **B)** Changes in expression of CD80 in M1 macrophages in different treatment groups of humanized YHIM-2004 PDX tumor, indicating that combination treatment significantly increased the expression compared to pembrolizumab treated group ($p$<0.05). **C)** Multispectral images of the tumor microenvironment in humanized YHIM-2004 PDX tumor. Multiplex images indicated that the tumor tissue had comparatively reduced in the CJRB-101 and combination treated group, and that abundance of myeloid-lineage cells in the tumor nest increased in the combination group. **D)** Abundance of M1 macrophages in the tumor nest and stroma generally increased by the combination treatment compared to the vehicle and monotherapy groups (left). In the total area of regions of interests (ROIs), average cell counts of M1 macrophages was significantly higher in the combination group compared to pembrolizumab and CJRB-101 treated group ($p$<0.0001 and $p$<0.05, respectively). Average counts of macrophages were generally higher in pembrolizumab treat group (right). **E)** Uniform Manifold Approximation and Projection (UMAP) plots were generated to display the integrated single cell profiles, colored by clusters. The C1_Macro/Mono/DC cluster was extracted and then processed after additional filtering for macrophages and monocytes. The expressions of the top 10 marker genes from the CJRB-101 treated group, the vehicle group and the pembrolizumab group were visualized for each group **(F)** and each cluster **(G)**. **H)** Enriched clusters of the CJRB-101 treated group, the vehicle group and the pembrolizumab group in macrophages and monocytes. **I)** Comparison of abundances between the enriched macrophage clusters of the CJRB-101 treated group (C1_Macrophage and C5_Macrophage) and the pembrolizumab group (C7_Macrophage). *P-values* were calculated from the t-test. **J**) Volcano plot represents gene expression differences between the enriched macrophage clusters of the CJRB-101 treated group and the pembrolizumab group. Each point represents a differentially expressed gene, with red points indicating genes with a significant change in expression. The horizontal dashed line marks statistical significance (*p-value* < 0.05), while the vertical dashed lines indicate fold change cutoffs (|log(fold change)| > 0.5).

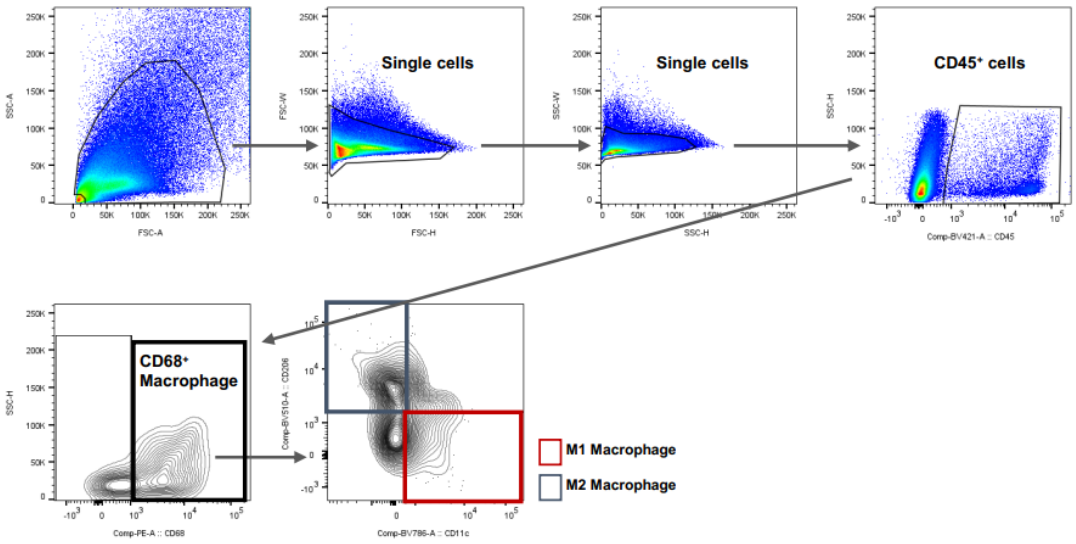


**Supplementary Figure S9. myeloid gating strategy.** Flow cytometry gating strategy used to define M1/M2 macrophages in humanized YHIM-2004 PDX model tumors

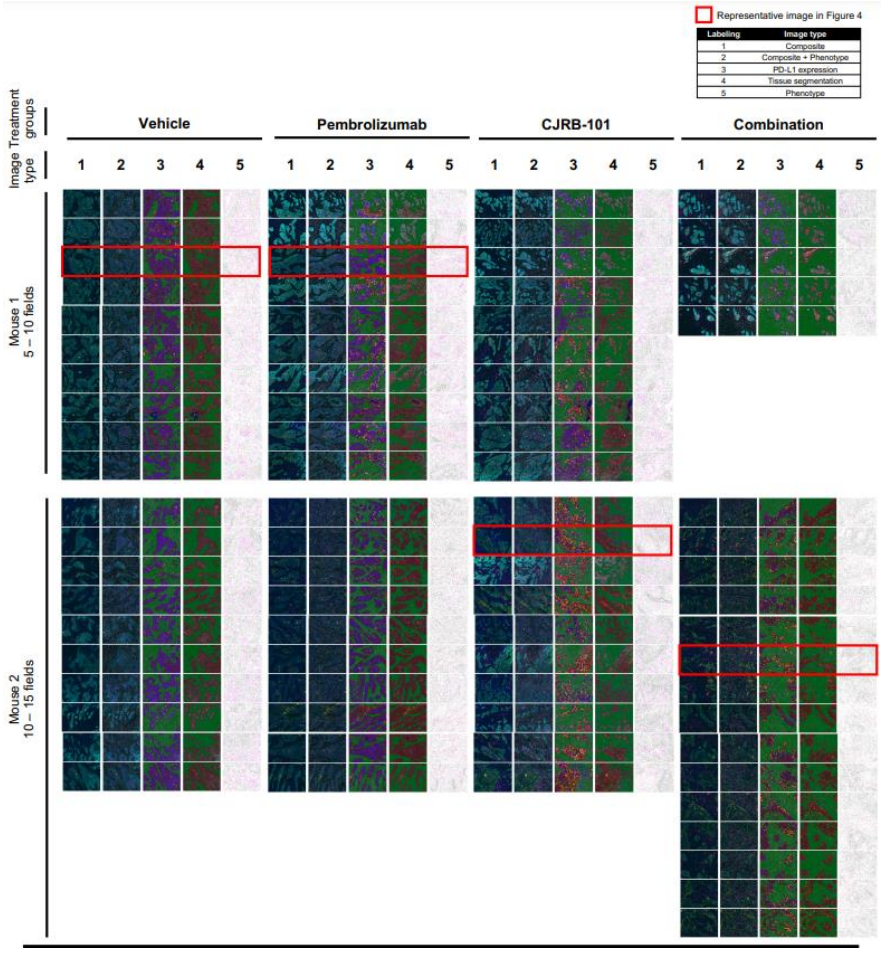


**Supplementary Figure S10. Multispectral images of myeloid panel in humanized YHIM-2004 PDX tumor.** M panel of Mouse 1 and 2 in each treatment group in 1) Composite image, 2) Composite + phenotype image, 3) PD-L1 expression image, 4) Tissue segmentation and 5) phenotype only image.

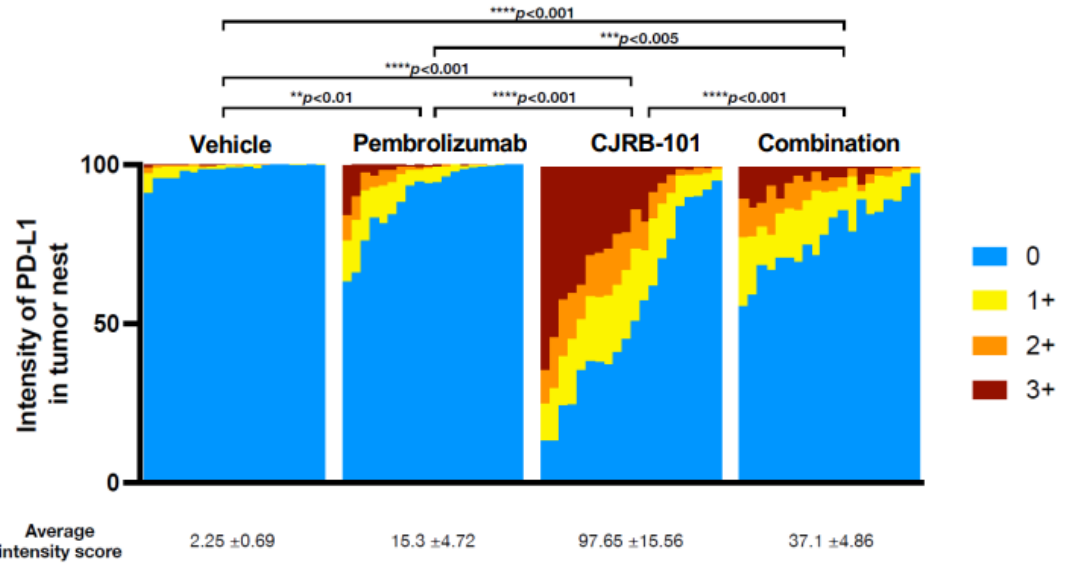


**Supplementary Figure S11. PD-L1 expression in tumor nest of myeloid panel in humanized YHIM-2004 PDX tumor**

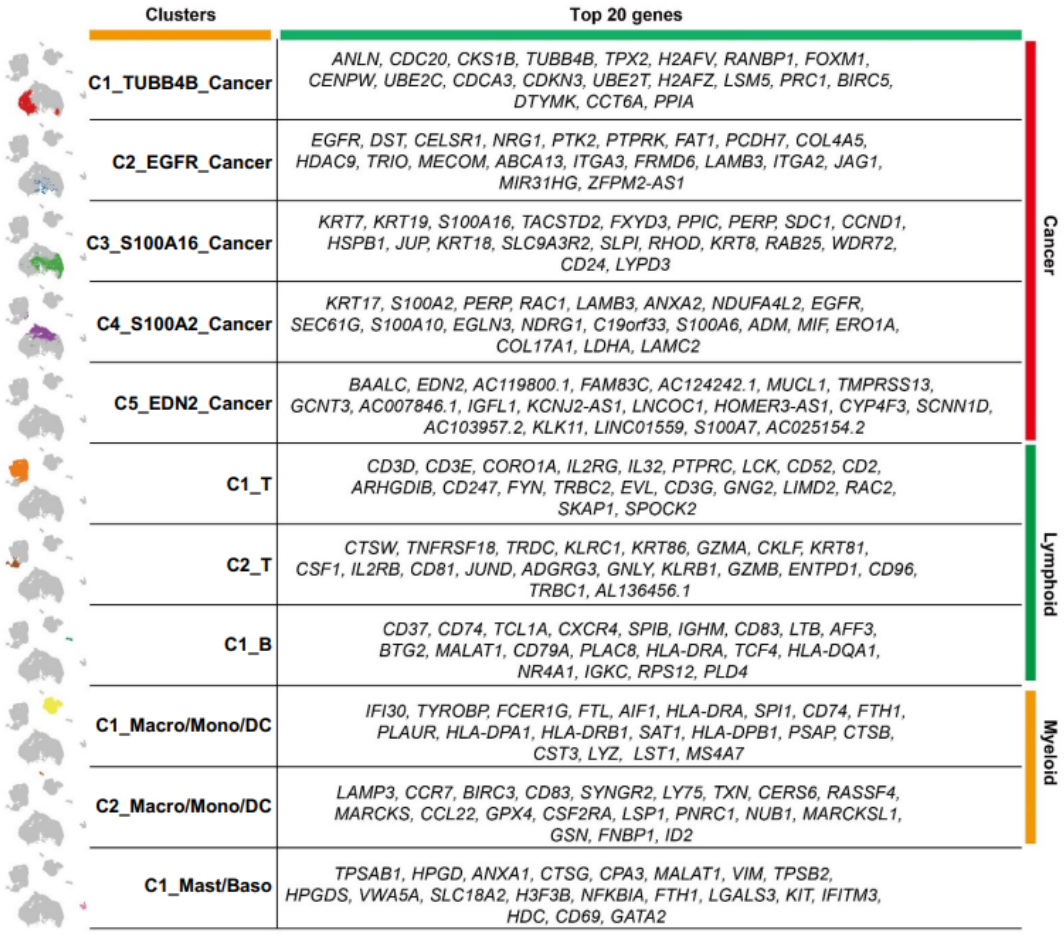


**Supplementary Figure S12. Top 20 marker genes for clusters across all cell types.** Marker genes from a total of 11 clusters are shown

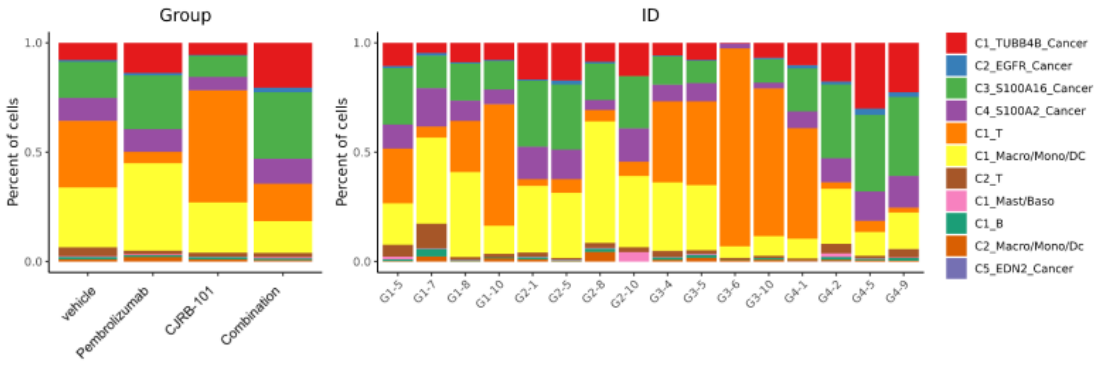


**Supplementary Figure S13. Cluster abundances across all cell types.** Cluster abundances by groups and samples were visualized.

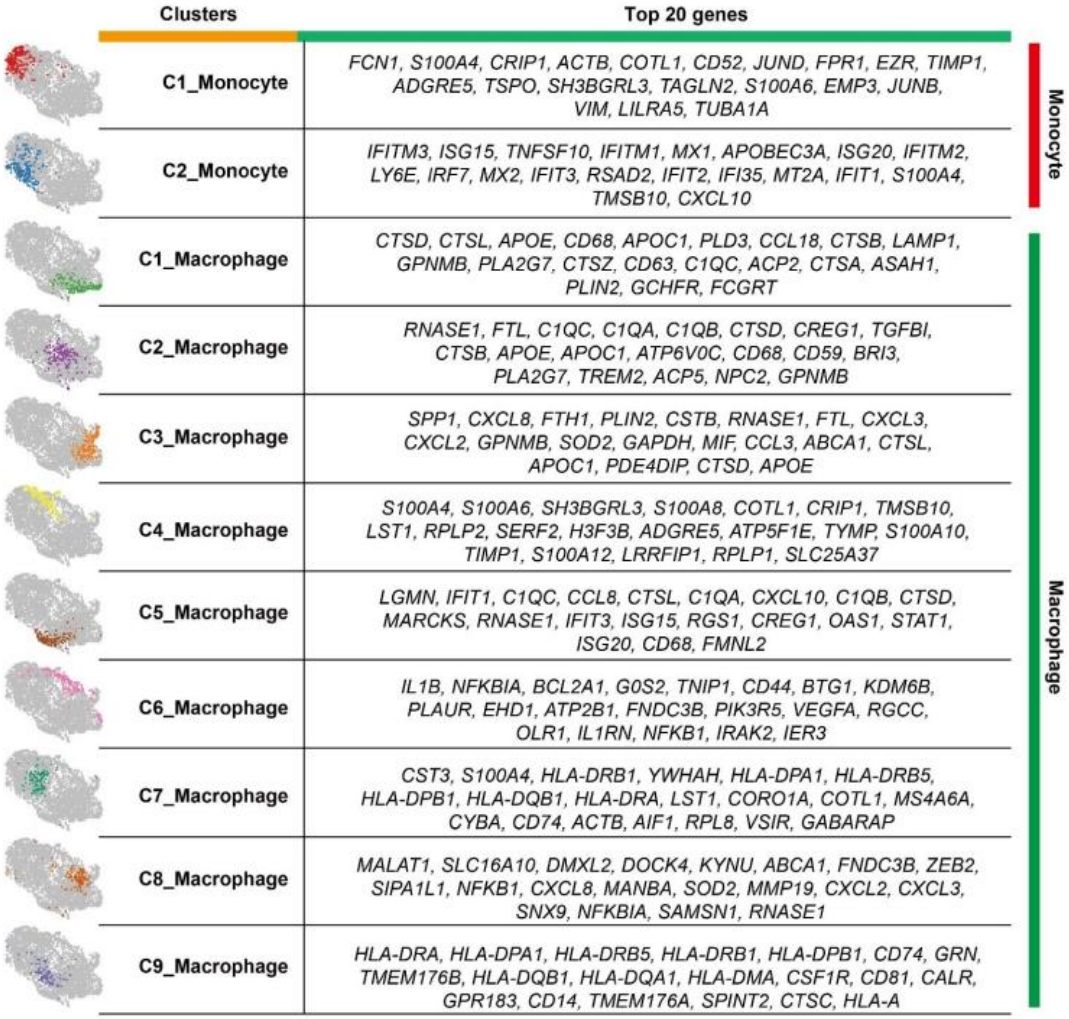


**Supplementary Figure S14. Top 20 marker genes for clusters in macrophages and monocytes.**
Marker genes from a total of 11 clusters are shown.

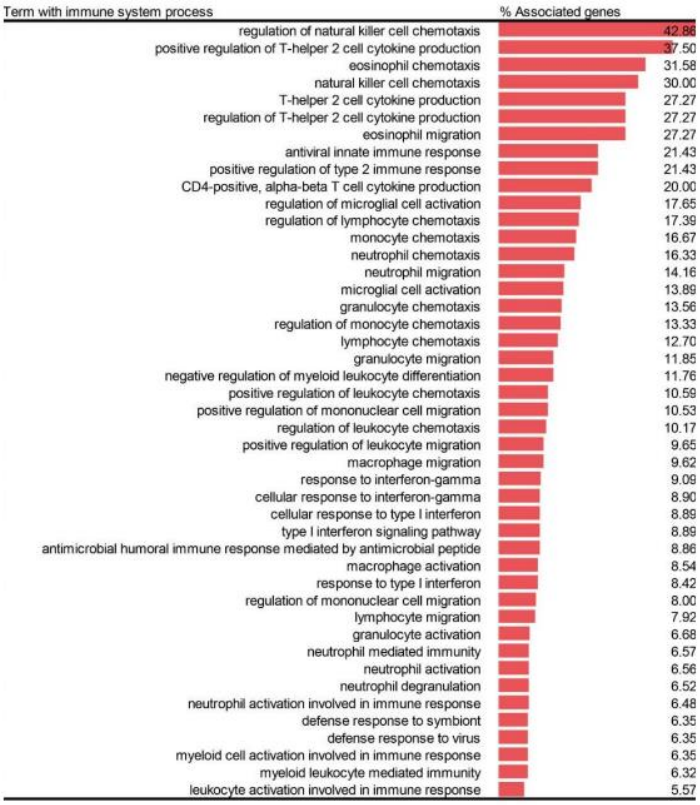


**Supplementary Figure S15. Gene enrichment analysis for up-regulated genes in CJRB-101-enriched macrophage clusters compared to the pembrolizumab-enriched macrophage cluster, focusing on the immune system process using ClueGO.** Features were sorted based on the percentage of associated genes.

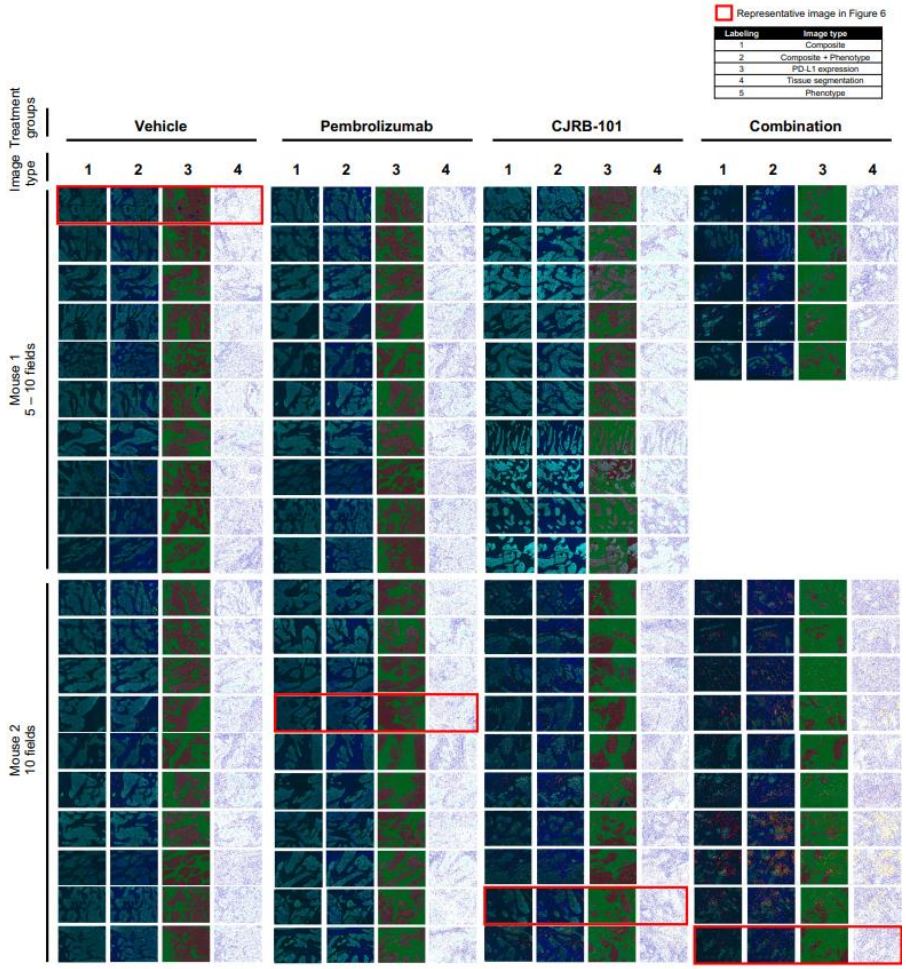


**Supplementary Figure S16. Multispectral images of T lymphocyte panel in humanized YHIM-2004 PDX tumor.** T panel of Mouse 1 and 2 in different treatment groups in 1) Composite image, 2) Composite + phenotype image, 3) Tissue segmentation and 4) phenotype only image.

### 3.5 CJRB-101 enhances infiltration of active $CD8^+$ $T_c$ cells into the tumor microenvironment

Based on previous results, we hypothesized that macrophages enhance the immune response to combination treatment by inducing phenotypic changes in the tumor-killing T lymphocytes in the TME. Flow cytometry analysis revealed that combination treatment enhanced the proportion of central memory subsets in $CD3^+$ T cells, inducing superior antitumor efficacy against tumor cells (26.1% ±11.2, Fig. 5A). It also significantly increased the expression of IFNγ in $CD8^+$ $T_c$ cells residing in the tumor compared to the vehicle group (1474.4 ±171.9 and 934.9 ±193.5, $p$<0.0001, Fig. 5B), indicating that the combination increased active proportion and killing capacity of $CD8^+$ $T_c$ cells within the TME. Multiplex imaging demonstrated that combination treatment enhanced the infiltration of activated tumor-killing T cells into the tumor site. The density of immune cells, including granzyme B (GRZB)-expressing $CD8^+$ ($T_c$) and $CD4^+$ ($T_h$) T cells, was dramatically increased in CJRB-101- and combination-treated tumors compared to the other treatment groups (Fig. 5D). The average cell counts of $GRZB^+$ $T_c$ cells in the total area of ROIs in the CJRB-101- and combination-treated groups were 68.15 and 63.07%, respectively, which were significantly higher than those in the pembrolizumab-treated group ($p$<0.0001, 3.5, Fig. 5D). The combination group had the highest count of $GRZB^+$ $T_h$ cells (313.5), which was significantly higher than that of pembrolizumab ($p$<0.0001, 8.5) and CJRB-101 treated groups ($p$<0.0001, 92.7, Fig. 5D). CJRB-101 in combination with pembrolizumab effectively reduced tumor growth in the YHIM-2004 PDX by augmenting the presence of active $CD8^+$ and $CD4^+$ T cells in the TME.

We specifically extracted T cell-related clusters (C1_T and C2_T) from the scRNA-seq data for a more detailed analysis of the T cells (Fig. 5E). After additional filtering for T cells, we identified 10 subclusters within this group, each characterized by unique marker genes (Fig. 5E, Supplementary Fig. S18). We identified the top 10 marker genes in the vehicle group, pembrolizumab group, and CJRB-101 treated group (Fig. 5F). Subsequently, we analyzed the expression patterns of these genes across each cluster (Fig. 5G). Notably, the C4-MKI67-Proliferating_T and C10-MKI67-Proliferating_T clusters showed higher expression of the marker genes in CJRB-101 treated group whereas the C2-CCL3-$T_c$ cluster predominantly expressed marker genes from the vehicle group (Fig. 5G, Fig. 5H). The C6-FCER1G-T cluster contained marker genes that were highly amplified in the pembrolizumab-treated group (Fig. 5G, Fig. 5H). We compared the abundance of enriched T cell clusters in CJRB-101 treated (C4-MKI67-Proliferating_T and C10-

MKI67-Proliferating_T) and pembrolizumab groups (C6-FCER1G-T) and found that the fraction of enriched T cell clusters in CJRB-101 treated group was significantly higher than that in the pembrolizumab group ($p$<0.05, Fig. 5I). Subsequently, we analyzed the gene expression profiles of these enriched T-cell clusters in both groups (Fig. 5J). Notably, the T cell clusters enriched in the CJRB-101 treated group had elevated expression levels of genes associated with both T cell exhaustion (LAG3 and PD-1) and T cell activation (IL2RA and IFNG; Fig. 5K, Supplementary Fig. S19).

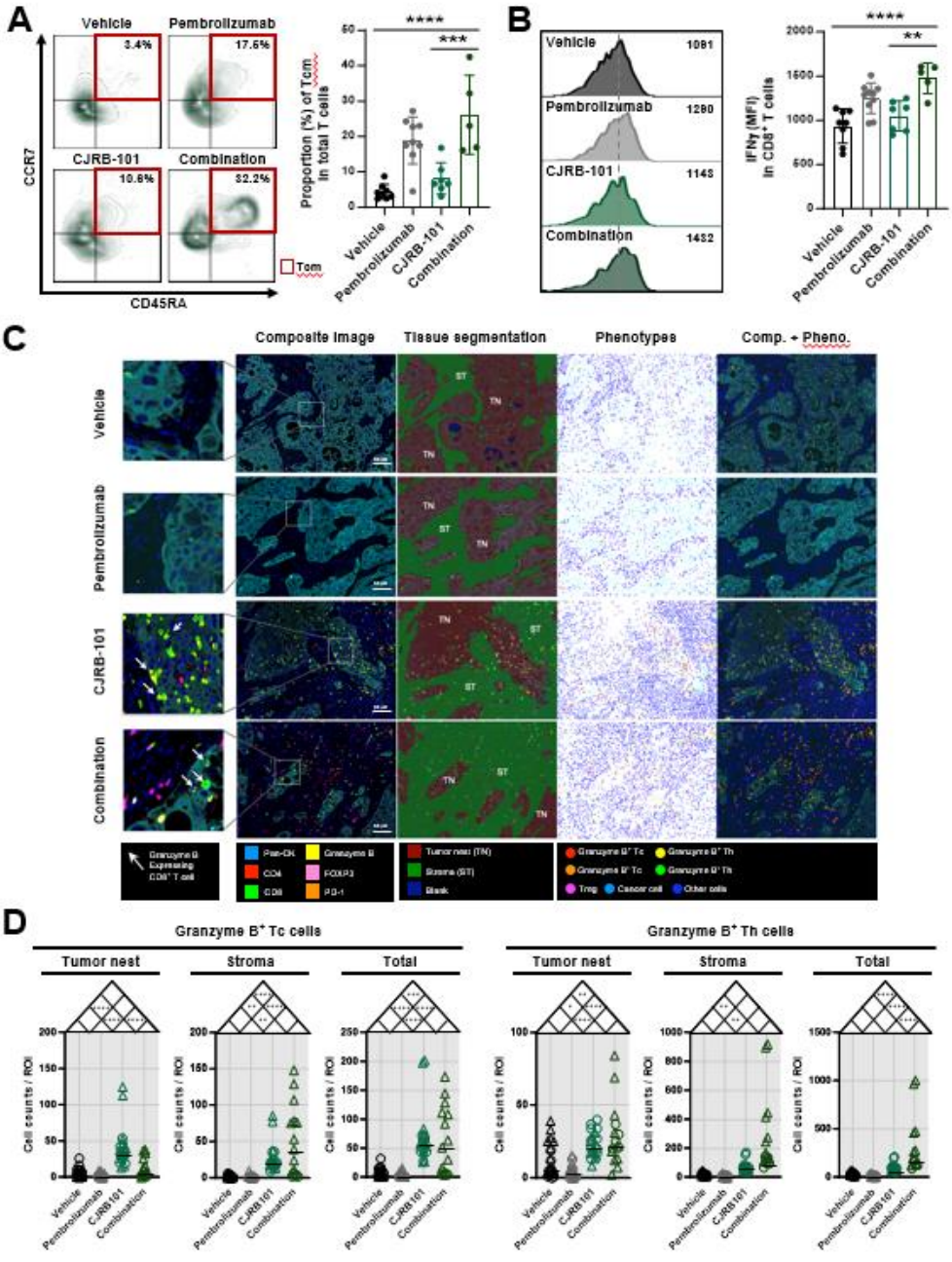

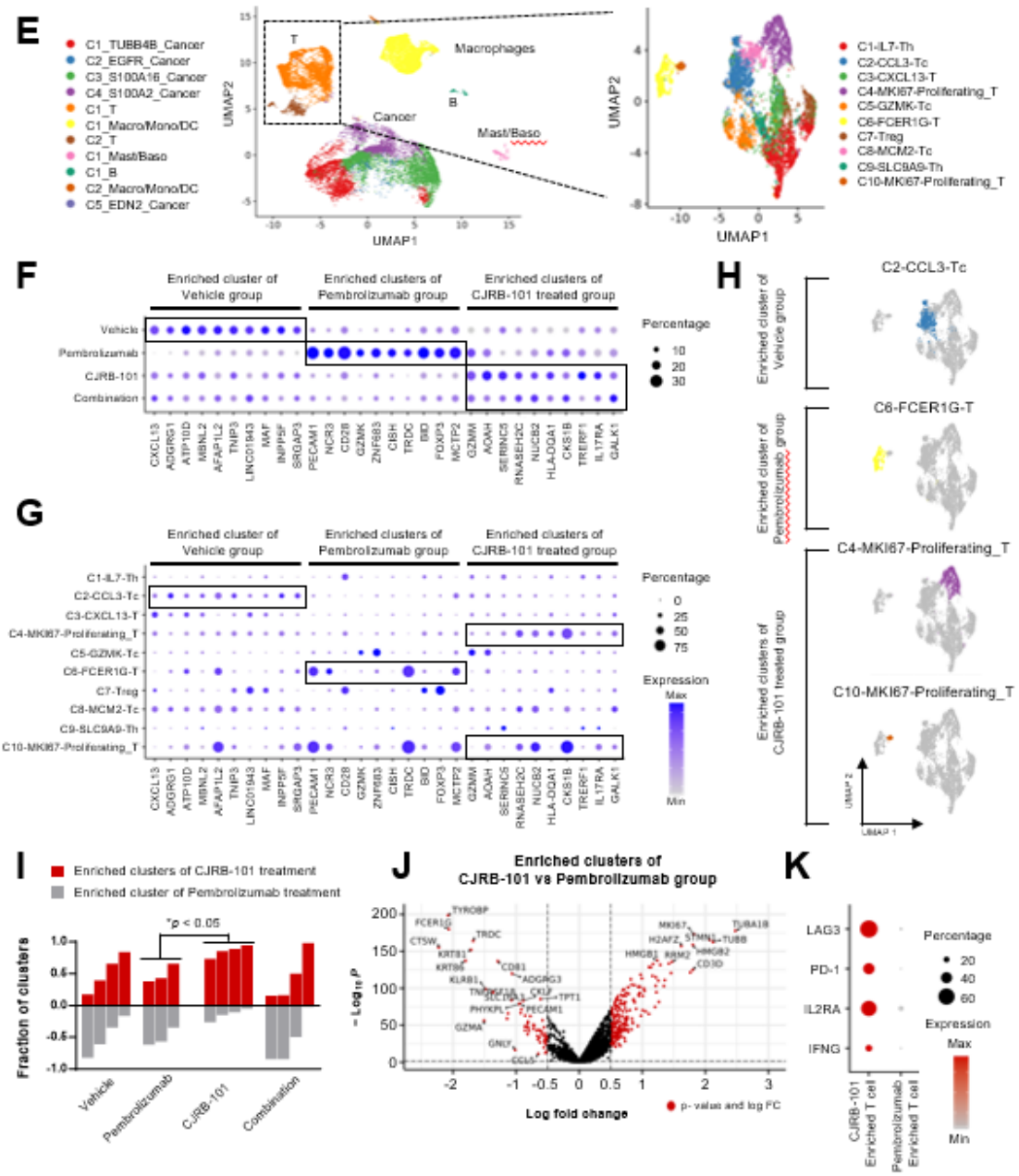

**Figure 5**. T cell-mediated anti-tumor effects of CJRB-101 in combination treatment for humanized NSCLC YHIM-2004 PDX model. **A)** Changes in the proportion of central memory T cells in humanized YHIM-2004 PDX tumor in different treatment groups, highlighting significant increase in the central memory subset by the combination treatment. **B)** Changes in the expression of IFNγ in $CD8^+$ $T_c$ cells in the tumor and spleen of humanized NSCLC YHIM-2004 PDX model. **C)** Multispectral images of the tumor microenvironment showing T lymphocytes in the tumor nest and stroma of YHIM-2004 PDX tumor. Multiplex images indicated that the abundance of granzyme B expressing $CD8^+$ $T_c$ cells in the tumor nest increased in the combination group. **D)** Cell counts of $GRZB^+$ $T_c$ ($CD\ 8^+$) cells in the regions of interests (ROIs) was generally higher in CJRB-101 and combination treated groups (left). In the total area of ROIs, average cell counts of $GRZB^+$ $T_c$ ($CD8^+$) cells in CJRB-101 and combination groups was significantly higher than pembrolizumab group ($p$<0.0001). Similar trend was observed in $GRZB^+$ $T_h$ ($CD4^+$) cells where the average counts in total ROIs in the combination group was significantly higher than pembrolizumab group ($p$<0.0001, right). **E)** Uniform Manifold Approximation and Projection (UMAP) plots were generated to display the integrated single cell profiles, colored by clusters. The C1_T and C2_T clusters were extracted and then processed after additional filtering for T cells. The expressions of the top 10 marker genes from the CJRB-101 treated group, the vehicle group and the pembrolizumab group were visualized for each group **(F)** and each cluster **(G)**. **H)** Enriched clusters of the CJRB-101 treated group, the vehicle group and the pembrolizumab group in T cells. **I)** Comparison of abundances between the enriched T cell clusters of the CJRB-101 treated group (C4-MKI67-Proliferating_T and C10-MKI67-Proliferating_T) and the pembrolizumab group (C6-FCER1G-T). *P-values* were calculated from the t-test. One sample from the pembrolizumab group was excluded because the total number of cells in C4-MKI67-Proliferating_T, C6-FCER1G-T and C10-MKI67-Proliferating_T was one. **J)** Volcano plot represents gene expression differences between the enriched T cell clusters of the CJRB-101 treated group and the pembrolizumab group. Each point represents a differentially expressed gene, with red points indicating genes with a significant change in expression. The horizontal dashed line marks statistical significance (*p-value* < 0.05), while the vertical dashed lines indicate fold change cutoffs (|log(fold change)| > 0.5). **K)** The expressions of genes related to T cell exhaustion (LAG3, PD-1) and T cell activation (IL2RA, IFNG) were visualized for the enriched T cell clusters of the CJRB-101 treated group and the pembrolizumab group.

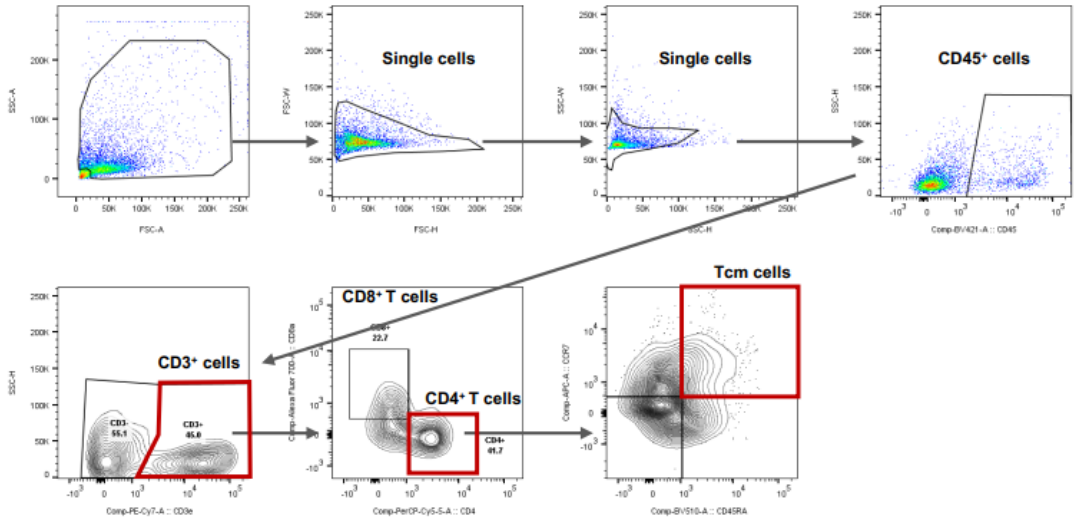


**Supplementary Figure S17.T cell gating strategy.** Flow cytometry gating strategy used to define central memory T cells in humanized YHIM-2004 PDX model tumors

| | Clusters | Top 20 genes |
|---|---|---|
|  | C1-IL7-Th | *IL7R, TCF7, KLF3, S1PR1, CD28, LEF1, RASA3, RASGRP2, TC2N, TSHZ2, TRAT1, TNFSF8, ANK3, PXN, SLC9A9, CRIP2, CCR7, SESN3, CD40LG, CYSLTR1* |
|  | C2-CCL3-Tc | *KIR2DL4, DBN1, KLRC2, IFITM10, CCL3, ITGA1, CD101, AFAP1L2, PDGFA, ADGRG1, HTRA1, TNFRSF9, ENTPD1-AS1, SRGAP3, CD9, GPR25, LAT2, MTURN, MCTP2, SHC4* |
|  | C3-CXCL13-T | *CXCL13, MFHAS1, RDH10, CD40LG, TSPAN13, LINC00892, GAB2, LAIR2, LINC01943, ATP10D, DPP4, PBX4, ETS2, TGIF1, IFNG, GK, NPDC1, LINC02694, VDR, GEM* |
|  | C4-MKI67-Proliferating_T | *MKI67, RRM2, NUSAP1, H2AFX, UBE2C, TYMS, TOP2A, HIST1H1B, KIF22, TPX2, CKS1B, PCLAF, CENPF, KIFC1, SMC4, SMC2, ZWINT, ASF1B, ASPM, HIST1H3D* |
|  | C5-GZMK-Tc | *ZNF683, GZMH, GZMK, CEBPD, MATK, TC2N, LYAR, SCML4, CCR5, F2R, CD70, GIMAP1, UBXN11, DDAH2, MCTP2, NELL2, RGL4, MT1F, STOM, ADA2* |
|  | C6-FCER1G-T | *TYROBP, FCER1G, TRDC, KRT86, KRT81, ADGRG3, PECAM1, FES, TMIGD2, CXXC5, LAT2, AREG, SCX, PLCG2, MCTP2, TXK, RNF130, APOC2, AFAP1L2, SH2D1B* |
|  | C7-Treg | *FOXP3, CD4, GADD45A, PTGIR, CD28, SATB1, PBX4, LTA, RTKN2, LY75, LINC01943, CCR8, FRMD4B, TBC1D4, PTP4A3, ZC3H12D, ADTRP, HTATIP2, HLF, LINC02694* |
|  | C8-MCM2-Tc | *TYMS, MCM2, GINS2, MCM4, FEN1, CDT1, PCLAF, CLSPN, UHRF1, E2F1, LIG1, HELLS, NCS1, TK1, IFITM10, DHFR, RRM1, CHAF1A, POLD2, WDR34* |
|  | C9-SLC9A9-Th | *SLC9A9, KIAA0825, ARL15, TSHZ2, ANK3, ZNF831, ST6GAL1, LINC02694, ZBTB20, TC2N, ZC3H12D, TTN, AC020916.1, TMEM131L, CAMK1D, IL6ST, RASA3, BTBD9, ATXN7, PLCL2* |
|  | C10-MKI67-Proliferating_T | *MKI67, TRDC, TYROBP, HIST1H1B, CENPF, UBE2C, FCER1G, CKS1B, NUSAP1, ADGRG3, TOP2A, AURKB, HIST1H3D, PECAM1, ASPM, RRM2, HIST1H3B, TPX2, KIFC1, CDK1* |

**Supplementary Figure S18. Top 20 marker genes for clusters in T cells.** Marker genes from a total of 10 clusters are shown.

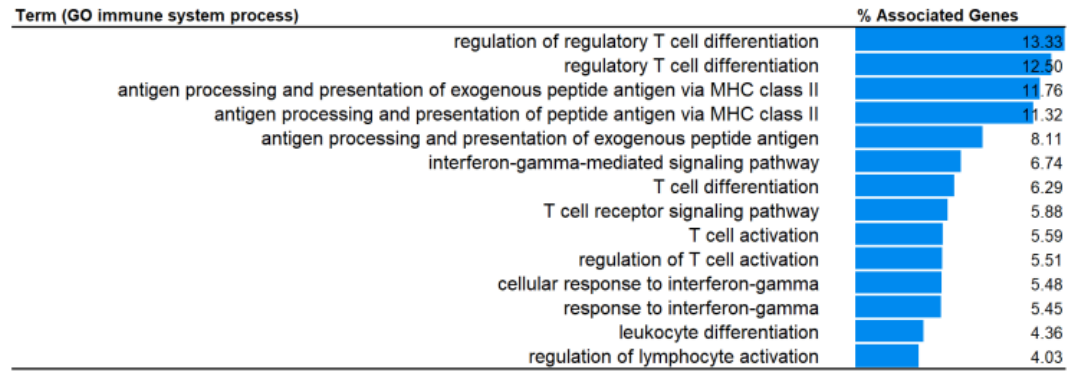


**Supplementary Figure S19. Gene enrichment analysis for up-regulated genes in CJRB-101-enriched T cell clusters compared to the pembrolizumab-enriched T cell cluster, focusing on the immune system process using ClueGO.** Features were sorted based on the percentage of associated genes.

### 3.6 Anti-tumor activity of CJRB-101 is mediated by macrophage-T cell activation via TLR4-dependent signaling

Using humanized PDX models, we confirmed that CJRB-101 exhibits an anti-tumor immune response through crosstalk between macrophages and $CD8^+$ $T_c$ cells. Analysis of the gut-TME axis was conducted to investigate the underlying antitumor mechanism of CJRB-101 and its influence on the TME. First, we validated the antitumor efficacy of the anti-PD-1 and CJRB-101 combination in a C3PQ syngeneic mouse model. Combination treatment effectively reduced tumor growth compared with treatment with anti-PD-1 alone (Fig. 6A). With vehicle as the standard of changes in tumor size, the combination group had -4.3 ±0.6 tumor reduction compared to the anti-PD-1 group with -0.8 ±1.4 a significantly reduction in tumor volume ($p$<0.001, Fig. 6A).

To identify the immune populations responsible for the anti-tumor effects of the combination treatment, depletion antibodies were administered in the C3PQ syngeneic mouse model (Fig. 6B). The results showed a significant increase in tumor size in the absence of CD8 (anti-CD8, 1492.3 $mm^3$ ±206.5) compared to the vehicle (864.0 $mm^3$ ±37.9, $p$<0.0001). The tumor size significantly increased when neutrophils/monocytes (anti-Ly-6G/Ly-6C, 1341.1 $mm^3$ ±192.2, $p$<0.001) and macrophages were depleted (anti-Macrophage, 1174.4 $mm^3$ ±83.9, $p$<0.05, Fig. 6B). Taken together, $CD8^+$ $T_c$ cells, neutrophils, and macrophages play a crucial role in the mechanism underlying the antitumor effects of CJRB-101 in combination with anti-PD-1.

To describe the immunological dynamics of local and systemic immune responses induced by the microbiome, we sampled organs at various time points using a syngeneic mouse model bearing the lung cancer cell line C3PQ. We collected samples from the gut (jejunum, colon), spleen, and tumor tissues to describe the changes in the gut-TME axis (Fig. 6C). To investigate the distribution of immune cells influencing the antitumor effects at various time points and in different organs, we sampled organs at multiple time points after anti-PD-1, CJRB-101, and combination treatments (Fig. 6C). The proportions were determined by setting each time point's vehicle group as a fold ratio, and comparisons were made to identify the most influential immune cell populations (Fig. 6D). Interestingly, macrophages and NK cells, associated with the innate immunity response, showed an increasing trend in the jejunum and colon, especially during the early days across various time points (day 3). Notably, in the combination treatment group, macrophages showed a significant increase in the jejunum at day 3 (9.4 ±1.9) and day 7 (12.6 ±2.4, Fig. 6D).

In the spleen, which represents systemic immunity, $CD8^+$ $T_c$ cells in the CJRB-101 and

combination groups started increasing on day 7 (1.6 ±0.1 and 1.8 ±0.2, respectively), peaking at day 10 (2.2 ±0.1 and 2.7 ±0.2, respectively). Furthermore, in the tumor, $CD8^+$ $T_c$ cells in CJRB-101 and the combination group increased on day 7 (2.5 ±0.3 and 2.8 ±0.3, respectively). Taken together, these results indicate that the combination treatment initiates the immune response with an early increase in innate immune cells, such as macrophages and NK cells. Subsequently, there is infiltration of $CD8^+$ $T_c$ cells in both systemic immunity and the tumor, leading to a sequential increase within the tumor.

ScRNA-seq analysis of NSCLC PDX tumors indicated that CJRB-101 induced immunomodulation of macrophages. Thus, we analyzed the trajectory of macrophages to observe trends in the CJRB-101 treated groups (Supplementary Fig. S21). Subsequent analysis revealed a trajectory from monocytes to the C1_Macrophage cluster, which was enriched cluster in CJRB-101 treated group (Supplementary Fig. S21). Along this trajectory, M2 expression increased first, followed by an increase in M1 expression. Thus, CJRB-101 may induce M2 to M1 repolarization.

Macrophage polarization and repolarization induced by CJRB-101 treatment under M2 differentiation conditions of bone marrow-derived macrophages (BMDM) were confirmed using macrophage markers by flow cytometry (Fig. 6E). Under dexamethasone-induced M2 conditions, CJRB-101 treatment led to a dose-dependent increase in M1 (EMR1, cell-only versus 1:1, $p<0.005$ versus 1:10, $p<0.001$) and MHC II (IA-IE, cell-only versus 1:1, $p<0.05$ versus 1:10, $p<0.001$) populations, with a significant reduction in the M2 (CD206) population (cell-only versus 1:1, $p<0.01$, versus 1:10, $p<0.005$). Thus, CJRB-101 induces M2 to M1 macrophage repolarization, as observed in the scRNA-seq analysis of the PDX tumor (Fig. 6E).

To identify the role of CJRB-101 in immune response, the cell wall (CW) and cell membrane (CM) of CJRB-101 were isolated and examined. M2 to M1 repolarization was assessed under dexamethasone-induced M2 conditions for each component (Fig. 6F). Compared to the average MFI of the dexamethasone treatment group (129), the level of MHC II (IA-IE) increased by 3.9 times with CW treatment (506.3) and by 11.8 times with CM treatment (1534.7, Fig. 6F). Moreover, the M1 (EMR1) population increased 2.2 times and 4.3 times in CW (1244.3) and CM (2356.3) treated group, respectively, compared to the vehicle group (dexamethasone group, 546.5). The M2 (CD206) population was confirmed to decrease by approximately 31.7% when treated with CW and by 57.3% when treated with CM, compared to the vehicle group. These findings confirmed that the most potent antigenic component of CJRB-101 resides in the cell membrane.

Transwell co-culture was used to confirm whether macrophages and T cells were activated by CJRB-101 CM using an ex vivo assay. CJRB-101 CM was co-cultured with tumor-associated macrophages (TAM) isolated from CT26 tumors, mouse splenocytes, and CT26 cells, and we observed an increase in the population of $CD8^+$ $T_c$ cells (cell only versus CM, $p<0.0001$, Supplementary Fig. S24). Subsequently, CJRB-101 CM was co-cultured with TAM isolated from CT26 tumors, $CD8^+$ $T_c$ cells isolated from naïve C57BL/6 mice, and CT26 cells were co-cultured with CJRB-101 CM. We found that the expression of CXCL9 significantly increased upon treatment with CJRB-101 CM compared to that in the untreated group (TAM+CD8 T versus TAM+CD8 T+CM, $p<0.01$). Furthermore, the dead cell population of CT26 cells was increased by CM (TAM+CD8 T versus TAM+CD8 T+CM, $p<0.05$, Fig. 6H). Treatment with CJRB-101 conditioned medium induced the activation of $CD8^+$ $T_c$ cells, leading to subsequent tumor-killing effects in an ex vivo assay mimicking the TME. Moreover, treatment with CJRB-101 increased the production of T cell-recruiting chemokines (CXCL9) in the supernatant. These results support the findings of the scRNA-seq analysis of chemokine-enriched macrophage clusters induced by CJRB-101.

The Toll-like receptor 4 (TLR4) signaling pathway regulates macrophage-mediated activation of T cells by CJRB-101. Further experiments confirmed that the markers showing differences upon CJRB-101 CM treatment were reduced by TLR4 antagonist (Fig. 6I). An in vitro experiment was conducted to investigate whether TLR4 signaling is implicated in the fate of macrophages induced by CJRB-101 CM (Fig 6I). TAK-242 (a TLR4 antagonist) significantly reduced the M1 marker (EMR1) increased by CJRB-101 CM (CJRB-101 CM vs. TAK-242 10 μM, $p<0.0001$ vs. TAK-242 20 μM, $p<0.0001$) in M2 macrophages. MHC II (IA-IE) levels were also significantly decreased by TAK-242 treatment in a dose-dependent manner ($p<0.0001$, CM only versus TAK-242). Moreover, the M2 marker (CD206), which was increased by dexamethasone, decreased after treatment with CJRB-101 CM. However, CD206 expression increased in a dose-dependent manner when treated with TAK-242 (CJRB-101 CM versus TAK-242 10 μM versus TAK-242 20 μM, $p<0.05$).

We also evaluated the anti-tumor efficacy of CJRB-101 CM *in vivo*. In the C3PQ syngeneic mouse model, when CM was administered with a TLR4 antagonist, the rate of change in tumor volume was significantly lower than when CM was administered alone (-4.1 ±1.2 and -7.1 ±0.8, respectively, $p<0.05$, Fig. 6J). Thus, cell membrane of CJRB-101 may be the dominant component inducing immunomodulation of macrophages through the TLR4 signaling pathway.

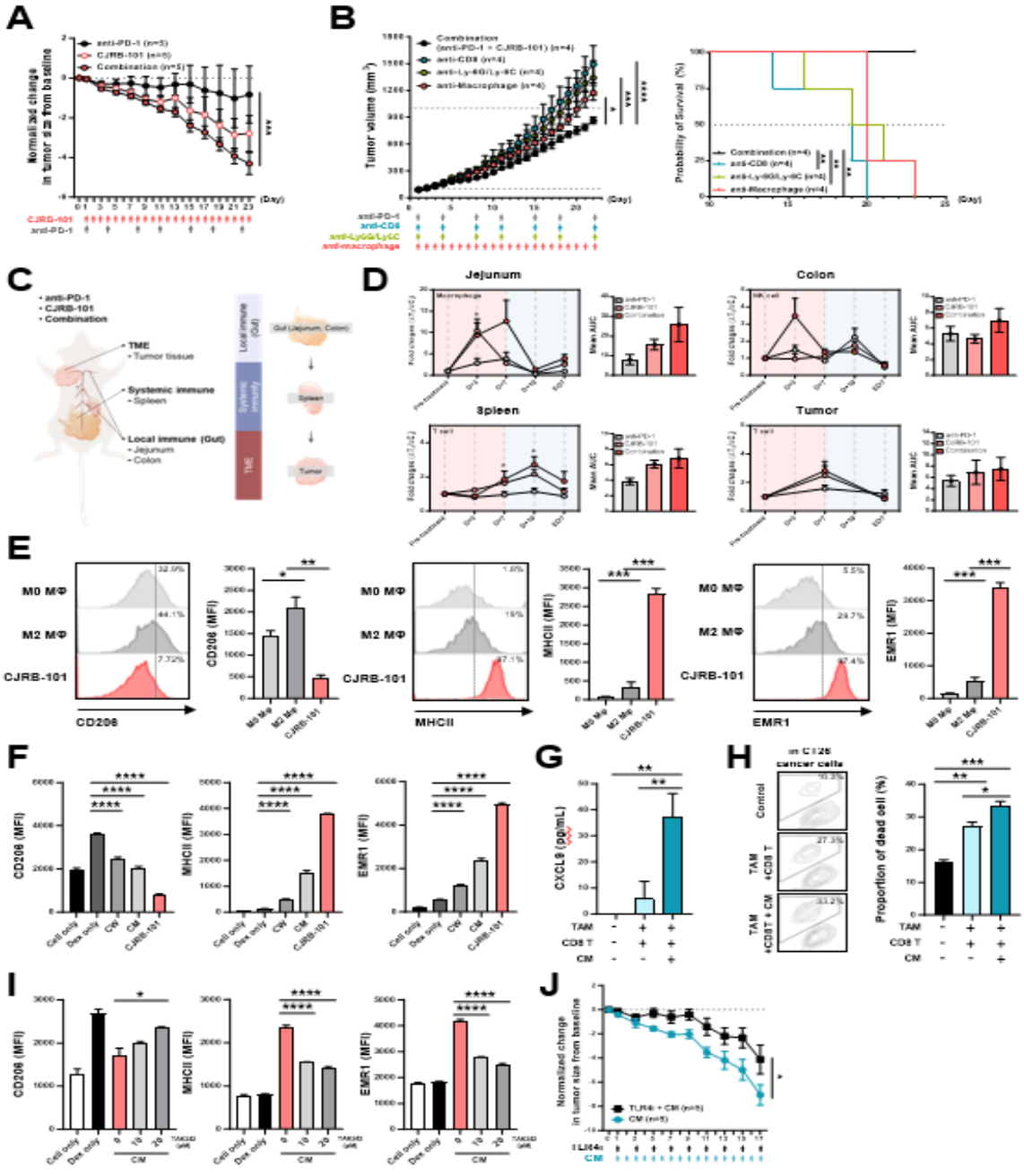

**Figure 6**. Immuno-profiling in gut-TME axis and potential mode of action of CJRB-101 through macrophage and $CD8^+$ $T_c$ cell. **A)** Normalized change in tumor size from baseline in C3PQ syngeneic mouse model. The tumor size in the combination group significantly decreased compared to the single treatment group. ($p$<0.001). **B)** Tumor volume and probability of survival (%) of immune cell ($CD8^+$ $T_c$ cell, Ly-6G/Ly-6C, Macrophage) depletion assay in C3PQ syngeneic model. The tumor size increased significantly in the CD8+ $T_c$ cell depletion group, followed by the Ly-6G/Ly-6C depletion group and the Macrophage depletion group, compared to the combination vehicle group ($p$<0.0001, $p$<0.001, $p$<0.05). **C)** Schematic overview of immuno-profiling in gut-TME axis. **D)** After anti-PD-1, CJRB-101, and combination treatment, organs were sampled at each time point (Day 3, 7, 10, EOT). Tumor tissues were obtained to confirm the immune population that most affects the anti-tumor effect in the tumor microenvironment, and gut (jejunum, colon) was obtained for local immune population. In addition, spleen was collected for system immunity. (Red area = innate immune stage, Blue area = adaptive immune stage). The early increase in macrophages and NK cells in the jejunum and colon shows the activation of the innate immune system. Subsequently, an increase in T cells was observed in the spleen and tumor**. E)** CJRB-101 induces M1 polarization and M2 to M1 repolarization in mouse bone marrow-derived macrophage (BMDM). **F)** M1 polarization and M2 to M1 repolarization in BMDM by cell wall and cell membrane of CJRB-101. **G)** and **H)** Secretion of CXCL9 and proportion of dead cell (%) in CT26 cancer in TME mimic ex vivo co-culture system. **I)** TLR4 antagonist (TAK-242; 0, 10, 20 μM) M1 polarization and M2 to M1 repolarization induced by cell membrane of CJRB-101 in BMDM. **J)** TLR4 depletion assay in C3PQ syngeneic mouse model.

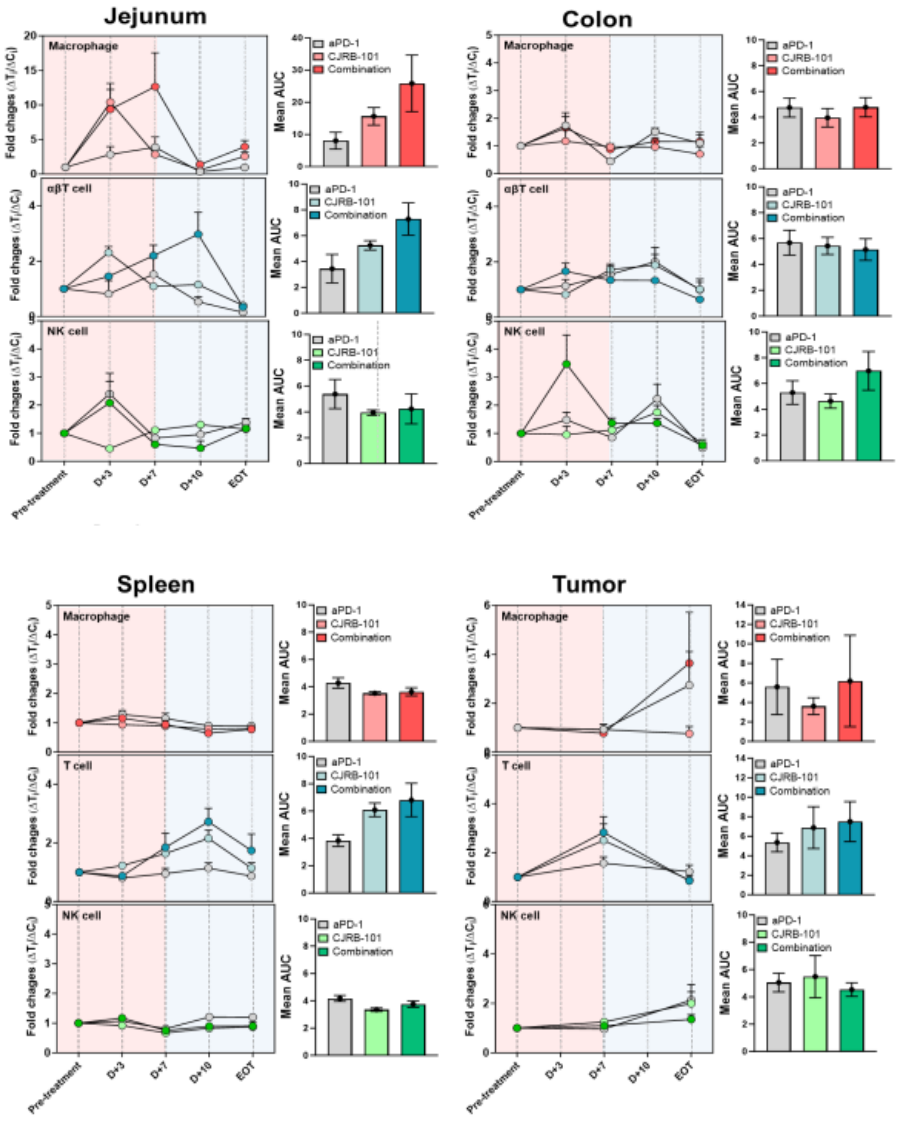


**Supplementary Figure S20. Immuno-profiling of gut-TME axis in C3PQ syngeneic mouse model.** After anti-PD-1, CJRB-101, and combination treatment, organs were sampled at each time point (Day 3, 7, 10, EOT). Tumor tissues were obtained to confirm the immune population that most affects the anti-tumor effect in the tumor microenvironment, and gut (jejunum, colon) was obtained for local immune population. In addition, spleen was collected for systemic immunity. (Red area = innate immune stage, Blue area = adaptive immune stage)

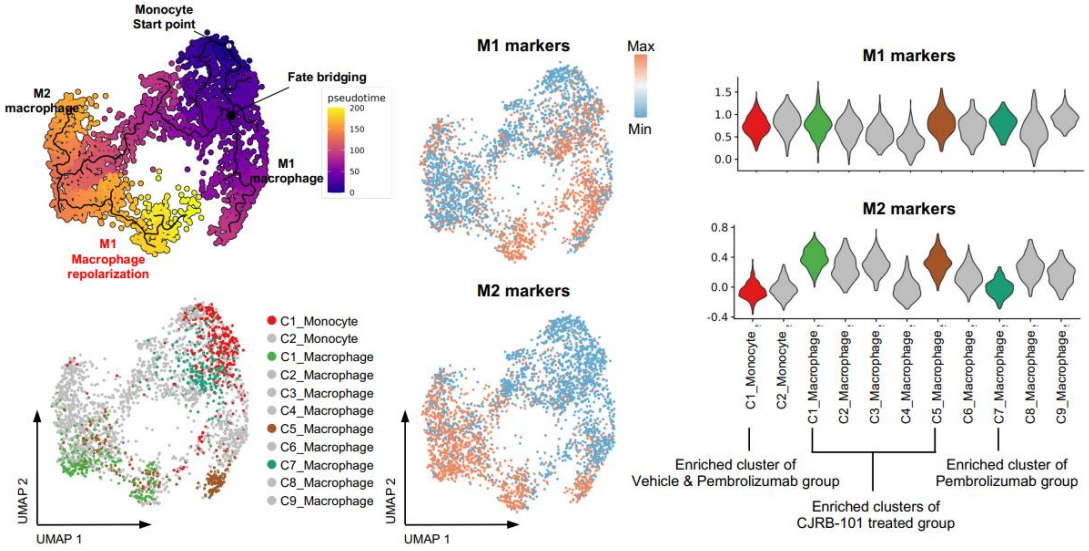


**Supplementary Figure S21. Single cell RNA sequencing data analysis for macrophages and monocytes.** Monocle 3 was used for constructing single-cell trajectories from monocytes to macrophages. Uniform Manifold Approximation and Projection (UMAP) plots were generated to display the integrated single cell profiles of macrophages and monocytes. Linear dimensional reduction was performed using a custom subset of features, including monocyte markers and marker genes for the macrophage cluster groups from the pembrolizumab and the combination group. M1 and M2 marker gene expressions were visualized on the UMAP plots after calculating module scores. M1 and M2 marker gene expressions were compared between clusters in macrophages and monocytes using the violin plots

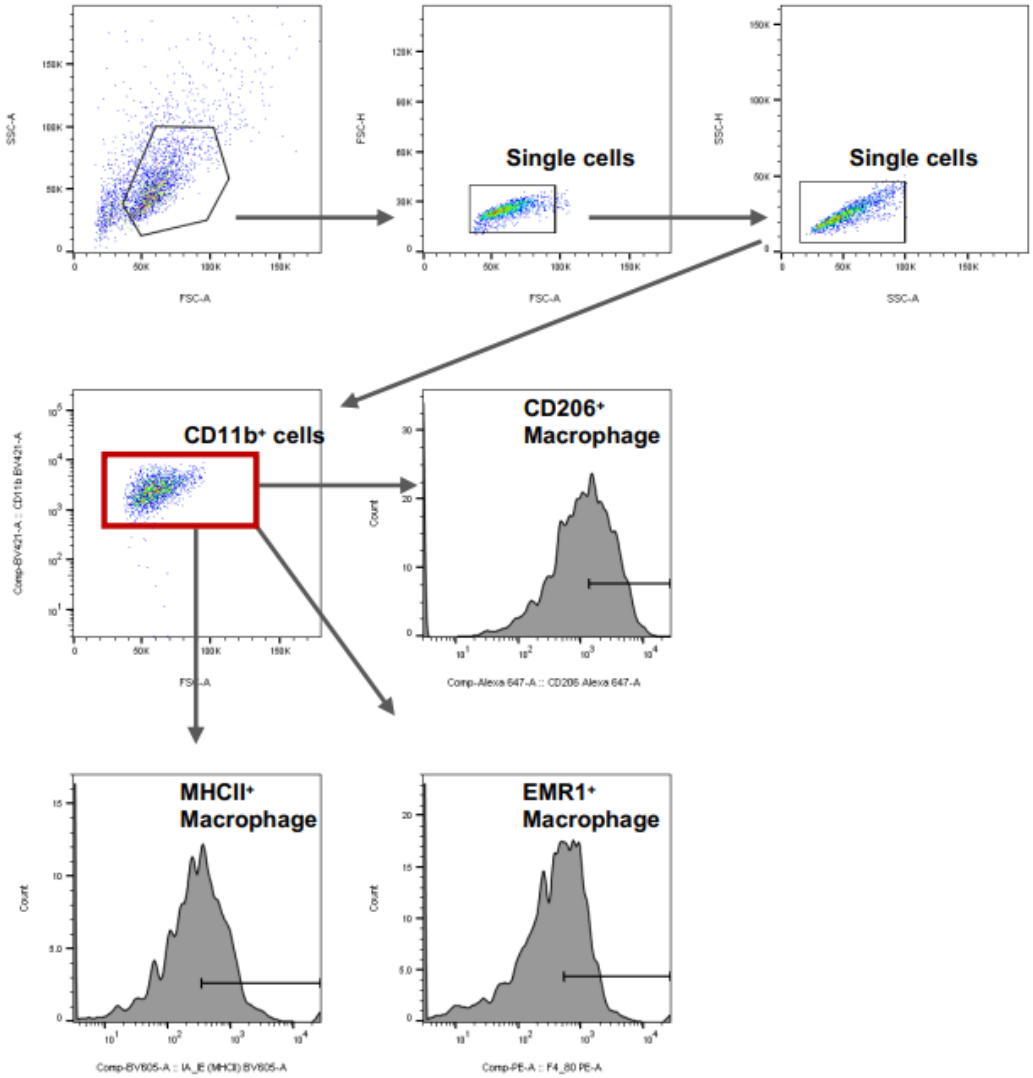


**Supplementary Figure S22. Macrophage gating strategy.** Flow cytometry gating strategy used to define M2 macrophage repolarization

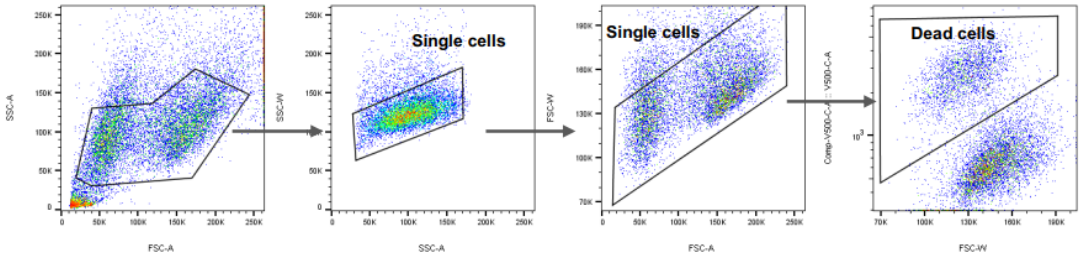


**Supplementary Figure S23. Dead cancer cell gating strategy.** Flow cytometry gating strategy used to count dead cell population.

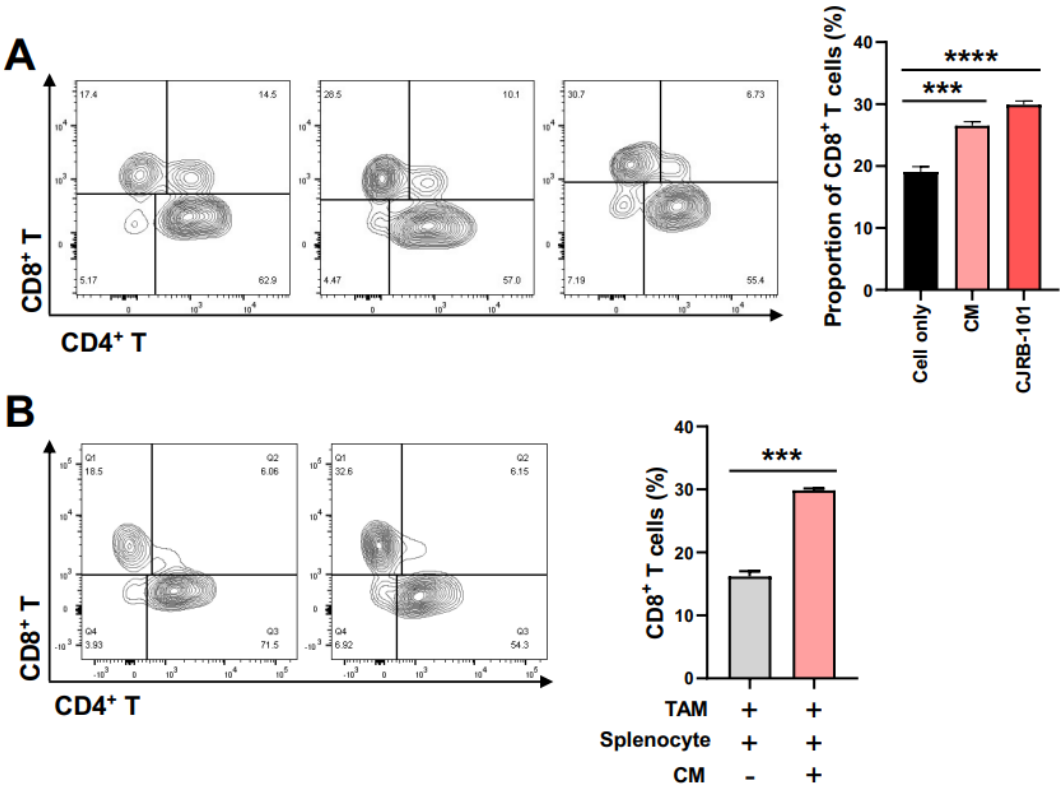


**Supplementary Figure 24. CD8$^+$ T$_c$ cell activation by CJRB-101 or cell membrane (CM). A)** CD8+ T$_c$ cell was activated by CJRB-101 and CM in mouse splenocyte.

**B)** CD8$^+$ T$_c$ cell was activated by CM in CT26 TAM, splenocyte co-culture system.

### 3.7 CJRB-101 in combination with pembrolizumab in treatment naïve metastatic NSCLC

As a clinical proof of concept, we investigated the anti-tumor activity in the phase 1/2 open label, safety and preliminary efficacy study of CJRB-101 in combination with pembrolizumab in solid tumors, including NSCLC (Fig. 7A). A 62-year old male with 40 pack-year smoking history was initially diagnosed with stage IV NSCLC and adenocarcinoma with PD-L1 70%. After two cycles of pembrolizumab with CJRB-101, the patient achieved a confirmed PR (-33%) without any safety issues (Fig. 7B). The combination of CJRB-101 with pembrolizumab is ongoing in other cohorts, including treatment-refractory metastatic NSCLC (NCT05877430).

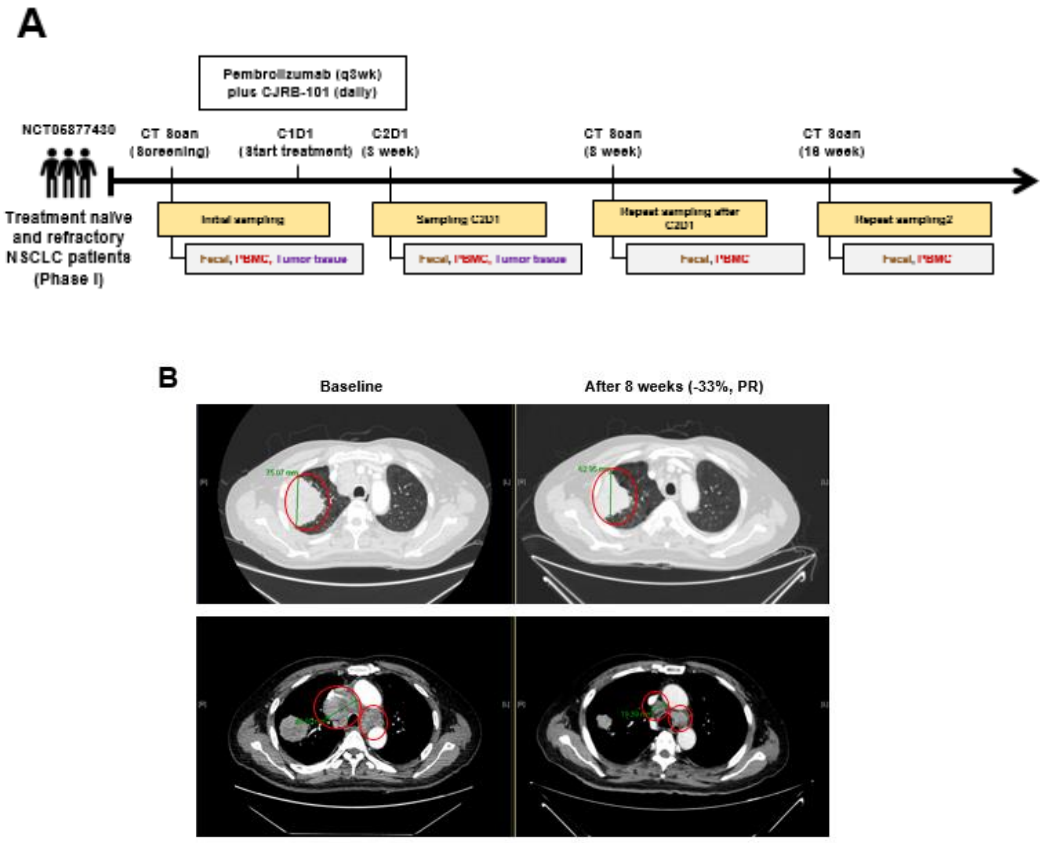


**Figure 7.** Clinical response of CJRB-101 in combination with pembrolizumab in treatment naïve NSCLC patient. **A)** Schematic overview of sample collection for combination with pembrolizumab treated naïve NSCLC patient. **B)** Confirmed partial response at 2 months with decrease of primary lung tumor, paratracheal lymph nodes. Red circles and green arrows indicate areas of metastatic tumor disease.

# 4. Discussion

In this study, CJRB-101 demonstrated potency by modulating macrophages for antitumor efficacy. CJRB-101 systemically boosts the immune response, ultimately leading to the repolarization of macrophages within the TME and enhancement of $CD8^+$ $T_c$ cell activity to eradicate tumor cells. In comparison with other agents that only activate T cells directly, CJRB-101 efficiently maintains significantly stronger anti-tumor efficacy over a long-term duration by modifying the TME towards immune-favorable conditions. CJRB-101 also creates a favorable environment for anti-tumor effects by immunoediting of the TME by modulation of macrophages favoring the pro-inflammatory M1 subset and ultimately transpiring into an increased influx of $CD8^+$ $T_c$ cells ($IFN\gamma^+GZMB^+$), contributing to anti-tumor immune responses. CJRB-101 was selected through comprehensive screening stages to identify strains that enhance IL-6 and IL-1β production (innate immune response) in mouse and human macrophage cell lines and increase $CD8^+IFN\gamma^+$ (adaptive immune response) in mouse splenocytes/human PBMC, a crucial indicator of anti-tumor immunity. Observations connecting the anti-tumor mechanisms of CJRB-101 with the activity of macrophages and T cells from scRNA-seq results using humanized PDX models and depletion experiments conferred that CJRB-101 was selected through well-established high-throughput screening (HTS).

CJRB-101 was a potent inducer of pro-inflammatory cytokines in macrophages during the selection process, and we found that CJRB-101 yielded robust anti-tumor effects in humanized NSCLC PDX models by modulation of macrophages and ultimately, tumor-killing CD8 $T_c$ cells in the TME. PDX models provide a number of advantages, with the most important factor being the ability to reproduce the TME of NSCLC tumors in an immune system that best replicates the cancer-immune cycle in humans. Therefore, our data may indicate the linkage of immune indicators as potential biomarkers in subsequent clinical trials.

Studies on the anti-tumor immune response of LAB within the *Lactobacillaceae* family have been reported in solid tumors, including colorectal and breast cancer (14-16). However, the current understanding of LBPs is limited at the cellular level, and in-depth analysis of the mechanism of action or development of therapeutic agents has not been conducted.

In addition, the association between the gut microbiome and response to immune checkpoint inhibitors (ICIs) has been reported (9,11,12), but taxa associated with response to immunotherapy varied, including *Akkermansia (12)*, *Bifidobacterium (9)*, and *Faecalibacterium*

*(11)*. The gut microbiome can vary depending on the demographic location (17) and diet (18), which may be one of the contributing factors to the observed differences in taxonomic features. To date, a variety of novel agents aimed at reprogramming macrophages into the M1 subset have been developed. Notably, compounds such as BLZ945 and LY3022855, which have been developed as CSF1R inhibitors, along with CD47-SIRPa inhibitors and CD40 agonists, are currently under development (19,20). TLR agonists targeting innate immune receptors have entered phase 1/2 clinical trials (21,22). In this regard, CJRB-101, as an orally administrable LBP-based antitumor agent, presents an intriguing innovation without perceived patient compliance issues or concerns.

# 5. Conclusion

In this study, we identified enterotypes in fecal samples of patients diagnosed with advanced NSCLC treated with pembrolizumab. As previously reported by Simpson et al. (2022), ICI responders were more prevalent in the *Oscillospiraceae*-dominated gut microbiome with high diversity (23). Similarly, we showed that the high-diversity enterotype had more responder-derived samples than the low-diversity enterotype. Taken together, the clinical response to pembrolizumab was positively correlated with microbial diversity, including a healthier gut state with higher values.

Our study provides a rationale for the first-in-human clinical trial of CJRB-101 plus pembrolizumab in various solid tumors, including both treatment-naïve and treatment-refractory advanced NSCLC (NCT05877430). Initial dosing in treatment-naïve metastatic NSCLC resulted in a 33% reduction in tumor size and regression of metastatic lymph nodes within 6 weeks. Further studies are ongoing to identify biomarkers in patients treated with this combination, including in-depth analyses of the immune-modulating responses of macrophages.

## References

1. Hanna NH, Temin S, Masters G. Therapy for Stage IV Non-Small-Cell Lung Cancer Without Driver Alterations: ASCO and OH (CCO) Joint Guideline Update Summary. Jco Oncol Pract 2020;16(8):E844-E8 doi 10.1200/Jop.19.00770.
2. Hiltbrunner S, Cords L, Kasser S, Freiberger SN, Kreutzer S, Toussaint NC, *et al.* Acquired resistance to anti-PD1 therapy in patients with NSCLC associates with immunosuppressive T cell phenotype. Nat Commun 2023;14(1):5154 doi 10.1038/s41467-023-40745-5.
3. Mountzios G, Remon J, Hendriks LEL, García-Campelo R, Rolfo C, Van Schil P, *et al.* Immune-checkpoint inhibition for resectable non-small-cell lung cancer - opportunities and challenges. Nat Rev Clin Oncol 2023;20(10):664-77 doi 10.1038/s41571-023-00794-7.
4. Hui R, Garon EB, Goldman JW, Leighl NB, Hellmann MD, Patnaik A, *et al.* Pembrolizumab as first-line therapy for patients with PD-L1-positive advanced non-small cell lung cancer: a phase 1 trial. Ann Oncol 2017;28(4):874-81 doi 10.1093/annonc/mdx008.
5. Garassino MC, Gadgeel S, Speranza G, Felip E, Esteban E, Dómine M, *et al.* Pembrolizumab Plus Pemetrexed and Platinum in Nonsquamous Non-Small-Cell Lung Cancer: 5-Year Outcomes From the Phase 3 KEYNOTE-189 Study. J Clin Oncol 2023;41(11):1992-+ doi 10.1200/Jco.22.01989.
6. Novello S, Kowalski DM, Luft A, Gumus M, Vicente D, Mazieres J, *et al.* Pembrolizumab Plus Chemotherapy in Squamous Non-Small-Cell Lung Cancer: 5-Year Update of the Phase III KEYNOTE-407 Study. J Clin Oncol 2023;41(11):1999-2006 doi 10.1200/JCO.22.01990.
7. Li X, Zhang SQ, Guo G, Han J, Yu J. Gut microbiome in modulating immune

checkpoint inhibitors. Ebiomedicine 2022;82 doi ARTN 10416310.1016/j.ebiom.2022.104163.

8. Frankel AE, Coughlin LA, Kim J, Froehlich TW, Xie Y, Frenkel EP, *et al.* Metagenomic Shotgun Sequencing and Unbiased Metabolomic Profiling Identify Specific Human Gut Microbiota and Metabolites Associated with Immune Checkpoint Therapy Efficacy in Melanoma Patients. Neoplasia 2017;19(10):848-55 doi 10.1016/j.neo.2017.08.004.
9. Matson V, Fessler J, Bao R, Chongsuwat T, Zha YY, Alegre ML, *et al.* The commensal microbiome is associated with anti-PD-1 efficacy in metastatic melanoma patients. Science 2018;359(6371):104-+ doi 10.1126/science.aao3290.
10. McQuade JL, Daniel CR, Helmink BA, Wargo JA. Modulating the microbiome to improve therapeutic response in cancer. Lancet Oncol 2019;20(2):E77-E91 doi Doi 10.1016/S1470-2045(18)30952-5.
11. Gopalakrishnan V, Spencer CN, Nezi L, Reuben A, Andrews MC, Karpinets TV, *et al.* Gut microbiome modulates response to anti-PD-1 immunotherapy in melanoma patients. Science 2018;359(6371):97-103 doi 10.1126/science.aan4236.
12. Routy B, Le Chatelier E, Derosa L, Duong CPM, Alou MT, Daillère R, *et al.* Gut microbiome influences efficacy of PD-1-based immunotherapy against epithelial tumors. Science 2018;359(6371):91-+ doi 10.1126/science.aan3706.
13. Chun J, Oren A, Ventosa A, Christensen H, Arahal DR, da Costa MS, *et al.* Proposed minimal standards for the use of genome data for the taxonomy of prokaryotes. Int J Syst Evol Microbiol 2018;68(1):461-6 doi 10.1099/ijsem.0.002516.
14. He Y, Wu W, Zheng HM, Li P, McDonald D, Sheng HF, *et al.* Regional variation limits applications of healthy gut microbiome reference ranges and

disease models. Nat Med 2018;24(10):1532-5 doi 10.1038/s41591-018-0164-x.

15. David LA, Maurice CF, Carmody RN, Gootenberg DB, Button JE, Wolfe BE, *et al.* Diet rapidly and reproducibly alters the human gut microbiome. Nature 2014;505(7484):559-63 doi 10.1038/nature12820.
16. Simpson RC, Shanahan ER, Batten M, Reijers ILM, Read M, Silva IP, *et al.* Diet-driven microbial ecology underpins associations between cancer immunotherapy outcomes and the gut microbiome. Nat Med 2022;28(11):2344-+ doi 10.1038/s41591-022-01965-2.
17. Zheng GXY, Terry JM, Belgrader P, Ryvkin P, Bent ZW, Wilson R, *et al.* Massively parallel digital transcriptional profiling of single cells. Nature Communications 2017;8 doi ARTN 1404910.1038/ncomms14049.
18. Bolyen E, Rideout JR, Dillon MR, Bokulich NA, Abnet CC, Al-Ghalith GA, *et al.* Reproducible, interactive, scalable and extensible microbiome data science using QIIME 2. Nat Biotechnol 2019;37(8):852-7 doi 10.1038/s41587-019-0209-9.
19. Callahan BJ, McMurdie PJ, Rosen MJ, Han AW, Johnson AJ, Holmes SP. DADA2: High-resolution sample inference from Illumina amplicon data. Nat Methods 2016;13(7):581-3 doi 10.1038/nmeth.3869.
20. Bokulich NA, Kaehler BD, Rideout JR, Dillon M, Bolyen E, Knight R, *et al.* Optimizing taxonomic classification of marker-gene amplicon sequences with QIIME 2's q2-feature-classifier plugin. Microbiome 2018;6 doi ARTN 9010.1186/s40168-018-0470-z.
21. Rognes T, Flouri T, Nichols B, Quince C, Mahe F. VSEARCH: a versatile open source tool for metagenomics. PeerJ 2016;4:e2584 doi 10.7717/peerj.2584.
22. Yoon SH, Ha SM, Kwon S, Lim J, Kim Y, Seo H, *et al.* Introducing EzBioCloud: a taxonomically united database of 16S rRNA gene sequences and whole-

genome assemblies. Int J Syst Evol Microbiol 2017;67(5):1613-7 doi 10.1099/ijsem.0.001755.

23. McMurdie PJ, Holmes S. phyloseq: an R package for reproducible interactive analysis and graphics of microbiome census data. PLoS One 2013;8(4):e61217 doi 10.1371/journal.pone.0061217.

24. Steinegger M, Soding J. MMseqs2 enables sensitive protein sequence searching for the analysis of massive data sets. Nat Biotechnol 2017;35(11):1026-8 doi 10.1038/nbt.3988.

25. Hyatt D, Chen GL, Locascio PF, Land ML, Larimer FW, Hauser LJ. Prodigal: prokaryotic gene recognition and translation initiation site identification. BMC Bioinformatics 2010;11:119 doi 10.1186/1471-2105-11-119.

26. Sivan A, Corrales L, Hubert N, Williams JB, Aquino-Michaels K, Earley ZM, *et al.* Commensal *Bifidobacterium* promotes antitumor immunity and facilitates anti-PD-L1 efficacy. Science 2015;350(6264):1084-9 doi 10.1126/science.aac4255.

Abstract in Korean

# 생균치료제인 CJRB-101의 진행성 비소세포폐암에서 대식세포-T세포 자극 및 항종양 활성의 역할

**연구 배경 및 목적:** 미생물군은 면역 체크포인트 억제제 (ICI)에 대한 반응에 영향을 미치지만, 진행성 비소세포 폐암 (NSCLC)에서 펨브롤리주맙 (Pembrolizumab)과 결합한 살아있는 생균치료제 (LBP)의 효과에 대해서는 알려진 바가 거의 없습니다. 본 연구는 높은 다양성의 장형 (high-diversity enterotype)이 치료를 받은 적이 없는 전이성 NSCLC에서 펨브롤리주맙에 대한 임상 반응과 관련이 있음을 확인하였습니다.

**연구 재료 및 방법:** 장내 미생물군의 면역 환경을 조절하기 위해 류코노스톡 메센테로이데스 (*Leuconostoc mesenteroides*)에 속하는 균주를 포함하는 살아있는 생균치료제 CJRB-101이 355개의 균주 중에서 선택되었습니다.

**연구 결과:** CJRB-101은 M2를 M1 대식세포로 재분극화하여 인간화된 NSCLC 환자 유래 이종이식 모델에서 종양 성장을 효과적으로 감소시켜 종양 미세환경 (TME)에서 활성 CD8+ Tc 세포를 향상시키고 내장-TME 축을 통해 적응 면역 시스템을 활성화 되는 것을 확인하였습니다. 종합하면, CJRB-101은 펨브롤리주맙과 결합한 잠재적인 치료 전략이며 현재 치료를 받지 않거나 치료 불내성 비소세포폐암 환자들을 대상으로 임상연구가 진행 중에 있습니다.

**결론:** CJRB-101은 대식세포의 LBP 주도 면역 조절에 의해 NSCLC에서 항종양 효과를 개선하고 장-TME 축을 통해 면역 세포의 종양 사멸 능력을 향상시킨다.

**핵심되는 말 :** CJRB-101, 생균치료제, 비소세포폐암, 면역항암제